UNIVERSITA' DEGLI STUDI DI CAGLIARI

Scuola di Dottorato in Scienze e Tecnologie Fisiche
Corso di Dottorato in Fisica della Materia

XX ciclo 2004-2007

Ph.D. Thesis in Physics

Photoluminescence Properties of Lanthanide doped Wide Gap Compounds of Interest in Photonics

Advisor:	Candidate:
Prof. Alberto Anedda	Dr. Marco Marceddu

Settore Scientifico Disciplinare FIS/01

Contents

Introduction

The subject of this Ph. D. thesis is the characterization of the photoluminescence properties of lanthanide doped wide band gap compounds of interest in photonics and optoelectronics.

Optical materials doped with rare earth elements are of great relevance in science and technology. Modern solid state optical technology is mainly based on lanthanide doped materials, with applications ranging from solid state lasers for industry, medicine and environmental monitoring, to active optical fibers for telecommunication purposes and phosphors for cathode ray tubes, displays, plasma monitors and lightning applications. From the scientific point of view, lanthanide doped materials attract increasing interest due to their particular physical properties. Indeed the electron configuration involving *f*-electrons and the exceptional time and space coherence properties lead to the observation of new and fascinating phenomena.

Among the materials currently evaluated as host for lanthanide ions, in this work our attention was focused on alkaline earth thiogallates. These materials are characterized by good transmission properties in the visible part of the electromagnetic spectrum and by relatively low phonon energies. They can be efficiently doped with lanthanide ions, due the similarity between the ionic radius of the alkaline earth and the lanthanide ions.

Therefore these materials are prospective high efficiency luminophors and are attracting increasing interest for photonics and optoelectronics applications. Indeed alkaline earth thiogallates are resistant to many chemicals and air exposure and can also be grown with low-cost techniques.

The samples studied in this work were grown with a solid state reaction technique at the Institute of Physics of Azerbaijan Academy of Sciences. Polycrystalline samples were characterized by means of time resolved photoluminescence measurements as a function of excitation wavelength between 250 and 400 nm, and as a function of temperature in the 10-335 K range. Phosphorescence and thermoluminescence properties were also investigated. In particular three main issues of basic research and technological relevance were addressed: the interactions between the rare earth elements (REE) and the thiogallate matrix, the interactions between the REE and the defects of the host, the interactions between REE in codoped samples.

This dissertation is organized as follows. In chapter 1 the main scientific and technological interests in optical materials activated with rare earth elements are briefly reviewed; in particular the main properties and some of the possible applications of alkaline earth thiogallates doped with lanthanides are presented. Chapter 2 deals with the interpretation of optical properties of lanthanide doped materials: energy levels determination, selection rules and broadening mechanisms are discussed in the framework of quantum mechanical theory. Moreover a brief review of the energy transfer processes between the lanthanide ions and the neighbour (i.e. the host lattice, co-dopant lanthanide ions or defects of the matrix) are presented. In the third chapter the measurements performed in this work are presented, with a description of the experimental set up and the sample growth technique. Experimental results are finally presented and discussed in chapters 4-7.

This work is part of the scientific collaboration between The Group of Optical Spectroscopy of The University of Cagliari, the P.N. Lebedev Institute of The Russian Academy of Science and the Institute of Physics of Azerbaijan Academy of Sciences.

Chapter 1: Rare Earths doped Optical Materials

1.1 Technological Interests in Rare Earths doped Optical Materials

The rare earth elements (REE) are characterized by the progressive filling of the 4*f* or 5*f* shells of their electronic configurations [1]. They occur in two groups known as lanthanides and actinides [2]. The lanthanides, which are associated with the filling of 4*f* shell, begin with cerium, end with lutetium and the atomic number ranges from 57 to 71 [2]. Actinides are instead characterized by the filling of 5*f* shell, with atomic number ranging from 90 (thorium) to 103 (lawrencium) [2].

The neutral lanthanides present the Xe electronic configuration, plus two or three outer electrons ($6s^2$ or $5d6s^2$). This electronic configuration determines the similarities in the chemical properties of the series [2]. The 4*f* electrons have wavefunctions that are compressed and shielded by the outer *s* and *p* closed shells [3, 4], that usually prevent any strong interactions of the 4*f* electrons with the environment [1]. Therefore intra-configurational 4*f* optical transitions are characterized by atomic-like absorption and emission lines. On the other hand the $4f^{n-1}5d$ electronic configuration is much more affected by the ligand neighbours, because of the larger extent of the wave function. Therefore inter-configurational $4f^{n-1}5d$ to $4f^{n}$ transitions are characterized by broad absorption and fluorescence bands [1,3,4].

The lanthanides are usually incorporated in crystals as divalent or trivalent cations for the realization of optically active materials [4] for photonic and optoelectronic applications. Indeed the particular electronic configuration leads to a variety of interesting optical properties [4] that are successfully used in commercial applications, and great effort is still devoted to the development of new materials and to the investigation of physical phenomena.

Specific applications may employ the rare earth's atomic-like $4f^{n}$ to $4f^{n}$ optical transitions when long lifetime, sharp absorption lines or coherence properties are required, while other applications may employ $4f^{n-1}5d$ to $4f^{n}$ transitions when large oscillator strength, broad absorption bands or fast response time are desirable [5]. Few examples of technological applications are listed in the following.

Nd^{3+} ions are widely used in active media for high power solid-state lasers [6]. Yttrium Aluminium Garnet doped with Nd^{3+} (Nd:YAG) is, by far, the most commonly used type of solid-state laser medium, because of the combination of properties uniquely favourable for lasing [6]. In Nd:YAG the lowest laser threshold occurs at 1064 nm, but laser effect is obtainable also at 946, 1319 and 1839 nm [6]. Other commercially available Nd based lasers use glasses as host matrix, SiO_2 and P_2O_5 in particular. Nd:$LiYF_4$

(Nd:YLF) exhibits lasing at 1053 nm and is commonly employed in Q-switched oscillators, amplifiers and for pumping purposes [6]. Gadolinium Scandium Gallium Garnet (GSGG) doped with Nd^{3+} is another attractive active medium, because its laser threshold cross section is about twice that of Nd:YAG [7].

Although no other dopant ions were as successfully applied as Nd^{3+} ions up to now, all of the trivalent lanthanide ions displayed laser properties [7]. The majority of these laser transitions are $4f$-$4f$ transitions with spectral features similar to that of Nd [7]. Broad-band fluorescence from the $4f^{n-1}5d$ to the $4f^{n}$ state of trivalent and divalent lanthanides can be employed to realize tunable vibronic lasers [6, 7]. This is the case of Ce:YLF and Ce:LaF_3 which exhibit laser emission at wavelengths of 325 and 286 nm respectively [6].

The lanthanide ions are also successfully employed in telecommunication applications. Erbium Doped Fiber Amplifiers (EDFAs) are used in long-range optical telecommunications to compensate the losses occurring in fibers [8, 9]. In an EDFA the Er- doped medium is pumped by laser diodes operating at 800-980 nm or at 1480 nm in order to achieve population inversion. The optical signals are thus amplified by stimulated emission [8]. Thulium doped fluoride fibers (TDFA) pumped around 1047 nm or 1400 nm can be used for amplification in the S band around 1460-1530 nm, while Pr doped fibers operating at 1300 nm are also available as amplifiers for the second telecom-window [9].

In the field of solid state light-emitting devices, an increasing interest is devoted to semiconductors activated with lanthanide ions [10-16]. Erbium-doped silicon nano-structures are investigated for 1.54 μm laser emission [10, 11], while organic-lanthanide ion complexes are studied as promising materials for new electro-luminescent devices [12, 13]. Cerium activated $CaGa_2S_4$ and $SrGa_2S_4$ thin films are regarded as one of the most promising pure blue phosphor materials and successfully used as thin film electroluminescent flat panel devices (TFEL) [14]. In addition laser oscillation was observed in several rare earth doped thiogallate compounds [15, 16].

Another important field of application of lanthanide doped materials concerns the realization of scintillators for high-energy radiation detectors for medical, industrial and scientific purposes. Scintillators absorb the energy from the high-energy particle, or radiation, and convert it into visible light that is detected by means of photomultiplier tubes or photodiodes [17]. Rare earths based scintillators employed Ce^{3+} $4f^{n-1}5d$ to $4f^{n}$ transitions, which are characterized by broad-band fluorescence with lifetime in the order of few tenth of ns, thus providing high light out-put and fast response time [18].

Lanthanide doped materials are also used as phosphors for lighting, cathode ray tubes (CRT's) and plasma displays [19, 20]. In energy-saving fluorescence lamps $BaMgAl_{10}O_{17}$:Eu, $(Ce,Gd,Tb)MgB_5O_{10}$ and Y_2O_3:Eu are employed as blue-, green- and red-emitting phosphors [21] while in CRT-based Projection Television (PTV) Y_2SiO_5:Tb is employed as a standard green phosphor [19, 20].

In the last decades a great effort was devoted to replace mercury-containing lamps with more environmentally safe solutions, such as noble gases, to develop more efficient phosphors for plasma display applications. This requires the use of phosphors with efficient excitation in the vacuum ultraviolet (VUV) and current researches indicate that such new phosphors could employ the down-conversion properties (quantum cutting) of lanthanide ions [19, 21-23].

The number of applications of rare earth doped optical materials constantly increases, together with the continuous improvement in the knowledge of their physical properties. Among the many fascinating challenges, a final citation pertains to the possibility of development of quantum storage devices, based on the extraordinary coherence properties of the hyperfine structure of lanthanide ions [24-26].

1.2 Alkaline Earths Thiogallates doped with Lanthanides

Among the large variety of materials that are currently investigated as hosts for rare earth dopants, our attention has been focused on alkaline earth thiogallates. Alkaline earth thiogallates doped with lanthanide ions are regarded as promising materials for optoelectronics and photonics applications, due to an attractive combination of favourable physical properties [27]: if compared to analogous binary compounds, these materials are characterized by a lower melting temperature (1100-1500 K), which offers the possibility to grow large size crystals of good quality [27]. Moreover alkaline earth thiogallates are stable in air and resistant to moisture and to different solvents, and thus are suitable for technological applications [27].

Alkaline earth thiogallates are ternary compounds with general formula MGa_2S_4 with M=Ca,Sr,Ba [28]. Calcium and Strontium Thiogallate ($CaGa_2S_4$ and $SrGa_2S_4$ respectively) crystallize in the orthorombic structure with space group D_{2h}^{24}-Fddd, while Barium Thiogallates ($BaGa_2S_4$) crystallizes in the cubic structure with space group Th^6-Pa3 [28]. In calcium and strontium thiogallates Ca and Sr cations occupy three different crystallographic sites in eightfold coordination with S anions [29-31]. These three sites are present in a ratio 1:1:2 with point symmetries D_2, D_2 and C_2 respectively [29]. In barium thiogallate instead, the Ba cations occupy two crystallographic sites with point symmetries C_{3i} and C_3 [32]. The main crystallographic data of these materials are summarized in table I.

compound	**crystal structure**	**lattice constants (Å)**			**space group**
		a	**b**	**c**	
$CaGa_2S_4$	orthorombic	20.087	20.087	12.112	D_{2h}^{24}-Fddd
$SrGa_2S_4$	orthorombic	20.840	20.495	12.212	D_{2h}^{24}-Fddd
$BaGa_2S_4$	cubic	12.660	12.660	12.660	Th^6-Pa3

Table I: crystallographic data of alkaline earth thiogallates, after Peters and Baglio [28].

The optical band gap of alkaline earth thiogallates ranges between 4.1 and 4.4 eV [32-34] and therefore these materials are characterized by good transmission properties in the visible part of the electromagnetic spectrum [27]. Moreover these materials are characterized by good conduction properties that allow acceleration of charge carriers up to optical energies under high electric field, enabling impact-excitation of luminescence centres [29]. Indeed these materials are commonly employed in electro-luminescent display applications [29, 35].

Alkaline earth thiogallates exhibit attractive properties as rare earth ions hosts. Indeed thiogallates can be doped with REE with concentrations up to 10^{21} cm^{-3}, due to the close values of REE's and alkaline earth's ionic radii [27]. The relatively large value of the band gap allows good emission properties [27], with high photoluminescence efficiency [36]. In fact the maximum phonon energy in alkaline earth thiogallates is at about 350 cm^{-1} [37], and, consequently, lanthanide ions photoluminescence is characterized by a low probability of multi-phonon non-radiative transitions [4, 36]. Moreover in MGa_2S_4 compounds, the lanthanide ions substitute the M cation in sites with low degree of symmetry [29]. Therefore a large number of transitions is expected, due to the removal of the lanthanide level degeneracy [36, 4].

The cathodoluminescence properties are also interesting, since the materials show a good linearity up to high current densities, making thiogallates suitable for field emission displays and TV projection [38].

Although alkaline thiogallate were doped with almost all the lanthanide ions [28, 29], the main part of research activity was devoted to the characterization of luminescence properties of Ce^{3+} and Eu^{2+} activated thiogallates, due to the possibility of TFEL, PTV and FED applications [40]. Ce^{3+} radiative transitions from the $4f5d$ (T_{2g}) to the ground state in MGa_2S_4 compounds occur with emission maximum at about 466, 448 and 442 nm and absorption maximum at about 425, 410 and 383 nm for M=Ca,Sr,Ba respectively [28, 41]. Beside the emission from the T_{2g} state of Ce^{3+} ions an UV emission at about 355 nm was observed in calcium thiogallate at low temperature, and attributed to radiative transitions from the E_g state to the ground state of cerium ions [42]. It was reported that the energy of the lowest 5*d* state of Eu^{2+} decreases while decreasing the size of the M cation from Ba to Ca [38]. Consequently photoluminescence ascribed to $4f^6 5d$ to $4f^7\left({}^8S_{7/2}\right)$ radiative transitions exhibit emission maxima at about 500, 530 and 560 nm for M=Ba,Sr,Ca respectively [35, 43-45]. Ce^{3+} and Eu^{2+} photoluminescence in alkaline earth thiogallates is characterized by an electron-phonon coupling of medium strength with characteristic vibronic emission bands [35, 44, 45]. Regarding fluorescence decay, Eu^{2+} fluorescence lifetime ranges between 300 and 600 ns depending on the temperature and the thiogallate matrix, while Ce^{3+} fluorescence lifetime is in the order of 10-25 ns [29, 38, 44, 45].

Beside Ce and Eu ions, Pr, Tb, Er, Tm, Nd were also investigated as active dopant for MGa_2S_4 compounds [29, 30, 46]. In $CaGa_2S_4$:Er a large number of intra-configurational 4*f*–4*f* radiative transitions have been observed between 400 and 1600 nm [30, 36]. Mid-infrared emissions in $CaGa_2S_4$:Er and $CaGa_2S_4$:Nd are characterized by high efficiency, due to the relative low phonon energy of the matrix, and by a fluorescence lifetime in the ms range suitable for laser applications [36, 46]. Moreover efficient energy transfer from the host lattice to the $^2H_{11/2}$ and $^4S_{3/2}$ levels of Er^{3+} was observed [36].

Well established applications of lanthanide doped alkaline earth thiogallates are TFEL, PTV, FED and light emitting diode (LED) devices [40, 47-49], but these materials are also evaluated for the development of new solid state lasers. In particular $CaGa_2S_4:Dy^{3+}$ exhibits tunable laser emission between 4.2 and 4.7 μm, with excitation energy threshold of a few mJ for lasing at 4.31 μm [15]. Calcium thiogallate has been also investigated as an high gain erbium host for laser emission at 1.6 μm [50], and $CaGa_2S_4:Ce^{3+}$(1% mol.) has been evaluated as active medium for solid state lasers [40]. In this material gain as higher as 37 cm^{-1} was measured from 450 to 530 nm, with increasing tuning range width by increasing the concentration of Ce^{3+} ions [40].

Although alkaline earth thiogallates doped with lanthanide ions have been studied since 1970's, they still attract interest both from the theoretical and experimental point of view. In particular great effort is devoted to the development of growth techniques, in order to overcome the difficulties of growing large single crystals and good quality thin films [31, 51]. In the last years many different techniques were considered and interesting results were obtained with molecular beam epitaxy (MBE), multi-source deposition

(MSD), horizontal Bridgman method and flash evaporation method [14, 34, 47, 51]. Great interest is also directed to theoretical calculation of lanthanide energy levels in the thiogallates matrix, and to the study of optical properties of undoped materials by first-principles techniques [52, 53, 41, 43].

Recently long lasting photoluminescence and thermoluminescence emissions were observed in lanthanide doped alkaline earth thiogallates [38, 54] and renewed interest is directed to the characterization of the photoluminescence kinetics [55]. In particular, different combinations of lanthanide ion dopants are investigated, in order to achieve an effective control of the long lasting emission properties [54, 56, 57].

References

[1] B. G. Wybourne *Spectroscopic Properties of Rare Earths* Interscience Pubblishing, New York 1965

[2] P. Silvestroni, *Fondamenti di Chimica* VIII edizione, Editoriale Veschi 1988, Milano

[3] G. H. Dieke *Spectra and Energy Levels of Rare Earths Ions in Crystals* Interscience Pubblishing, New York 1968

[4] J. Garcia Solè, L.E. Bausà, D. Jacque *An Introduction to the Optical Spectroscopy of Inorganic Solids*, Wiley 2005

[5] C. W. Thiel, PhD thesis, Montana State University, 2003

[6] W. Koechner *Solid-State Laser Engineering* 4th edition, Springer

[7] R. P. Powell *Physics of Solid-State Laser Materials,* AIP press-Springer

[8] A. Cutolo, *Optoelettronica-Ottica, fotonica e laser*, Mc Graw Hill 1997

[9] Encyclopedia of Laser Physics and Technology http://www.rp-photonics.com/encyclopedia.html

[10] A. Hryciw, C. Blois, A. Meldrum, T. Clement, R. DeCorby, Quan Li , Optical Materials 28 (2006) 873–878

[11] M.V. Stepikhova, L.V. Krasil'nikova, Z.F. Krasil'nik , V.G. Shengurov , V.Yu. Chalkov , D.M. Zhigunov, O.A. Shalygina, V.Yu. Timoshenko , Optical Materials 28 (2006) 893–896

[12] A. Edwards, C. Claude, I. Sokolik, T. Y. Chu and Y. Okamoto, R. Dorsinville, J. Appl. Phys. 82 (4), pp. 1841-1846

[13] Zheng Chen, Zhenbo Deng, Yumeng Shi, Ying Xu, Jing Xiao, Yuanyuan Zhang, Ruifen Wang, Journal of Luminescence 122–123 (2007) 671–673].

[14] A. Bayramov, H. Najafov, A. Kato, M. Yamazaki, K. Fujiki, Md. Nazri, S. Iida, Journal of Physics and Chemistry of Solids 64 (2003) 1821–1824

[15] M. C. Nostrand, et al., Opt. Lett. 24, 1215 (1999).

[16] S. Ida, T. Matsumoto, N. T. Mamedov, G. An, Y. Maruyama, A. I. Bairamov, B. G. Tagiev, O.B. Tagiev, and R. B. Dzhabbarov, Jpn. J. Appl. Phys., Part 2 36(7A), L857–L859 (1997)

[17] K. S. Krane *Introductory Nuclear Physics* Wiley 1988

[18] *Wide-Gap Luminescent Materials: Theory and Applications*, edited by S. R. Rotman, Kluwer Academic Publishers 1997

[19] R. T. Wegh, H.Donker, K. D. Oskam, A. Meijerink, Science vol. 283 pp 663-666 (1999)

[20] G. Bizarri, B. Moine, JOURNAL OF APPLIED PHYSICS 98, 113528 (2005)

[21] C.R. Ronda, J. All. Compounds 225, 534 (1995)

[22] Hsin-Yi Tzeng, Bing-Ming Cheng, Teng-Ming Chen, J. Lumin. 122-123, 917 (2007)

[23] P. Vergeer, T. J. H. Vlugt, M. H. F. Kox, M. I. den Hertog, J. P. J. M. van der Eerden, and A. Meijerink, Phys. Rev B 71, 014119 (2005)

[24] O. Guillot-Noel, Ph. Goldner, E. Antic-Fidancev, A. Louchet, J.L. Le Gouet, F. Bretenaker, I. Lorgere´ Journal of Luminescence 122–123 (2007) 526–528

[25] V. G. Kravets Optical Material 16 (2001) 369-375

[26] Ph. Goldner a, O. Guillot-Noel, A. Louchet , F. de Seze , V. Crozatier, I. Lorgere, F. Bretenaker , J.L. Le Gouet Optical Materials 28 (2006) 649–654

[27] A. N. Georgobiani, B. G. Tagiev, O. B. Tagiev, R. B. Diabbarov, N. N. Musaeva, U.F. Kasumov, Jpn. J. Appl. Phys. Vol 39 (2000) suppl. 39-1 pp. 434-439

[28] T. E. Peters, J. A. Baglio, J. Electrochem. Soc.: Solid-State Science and Technology 119 (1972) 230-235

[29] A. Bessiere, P. Dorenbos, C. W. E. Van Eijk, E. Yamagishi, C. Hidaka, T. Takizawa, Journal of The Electrochemical Society 151 (12) H254-H260 (2004)

[30] A. N. Georgobiani, A. N. Grunzitsev, C. Barthou, P. Benalloul, J. Benoit, B. G. Tagiev, O. B. Tagiev, R. B. Dzhabborov, Journal of The Electrochemical Society 148 (11) H167-H170 (2001)

[31] T. Takizawa, C. Komatsu-Hidaka, K. Asaka, T. Isomoto, H. Matsushita, Jpn. J. Appl. Phys. Vol 39 (2000) suppl. 39-1 pp. 35-40

[32] Mi-Yang Kim, Wha-Tek Kim, Moon-Seog Jin, Sang-An Park, Sung-Hyu Choe, Choong-Il Lee, Chang-Dae Kim, Juournal of Physics and Chemistry of Solids 64 (2003) 625-629

[33] N. Mamedov, S. Ida, H. Toyota, T. Aoki-Matsumoto, A. Kato, B. Tagiev, O. Tagiev, R. Dzhabarov, N. Yamamoto, T. Shishido, Jpn. J. Appl. Phys. Vol 39 (2000) suppl. 39-1 pp. 287-289

[34] T. Yang, B. K Wagner, M. Chaichimansour, W. Park, Z. L. Wang, C. J. Summers, J. Vac. Sci. Technol. B 14(3) 1996 pp. 2263-2266

[35] A. N. Georgobiani, V. V. Styrov, V. I. Tyutyunnikov, B. G. Tagiev, O. B. Tagiev, R. B. Djabbarov, Journal of Physics and Chemistry of Solids 64 (2003) 1519-1524

[36] A. Garcia, C. Foussier, Journal of Luminescence 24/25 (1981) 743-746

[37] C. Chartier, R. Jabbarov, M. Jouanne, Jean-Francois Morhange, P. Benalloul, C. Barthou, Jean-Marc Frigerio, B. Tagiev, E. Gambarov, J. Phys.:Condens Matter 14 (2002) 13693-13703

[38] P. Benalloul, C. Barthou, C. Foussier, A. N. Georgobiani, L. S. Lepnev, Y. N. Emirov, A. N. Gruzintsev, B. G. Tagiev, O. B. Tagiev, R. B. Jabbarov, Journal of The Electrochemical Society 150 (1) G62-G65 (2003)

[39] C. Hidaka, E. Yamagashi, T. Takizawa, Journal of Physics and Chemistry of Solids 66 (2995) 2061-2064

[40] S. Iida, T. Matsumoto-Aoki, T. Morita, N. Mamedov, B. G. Tagiev, F. M. Gashimzade, K. Sato, Jpn. J. Appl. Phys. Vol 39 (2000) suppl. 39-1 pp. 429-433

[41] P. Dorenbos, Journal of Luminescence 91 (2000) 155-176

[42] A. Kato, M. Yamazaki, H. Najafov, K. Iwai, A. Bayramov, C. Hidaka, T. Takizawa, S. Iida, Journal of Physics and Chemistry of Solids 64 (2003) 1511-1517

[43] P. Dorenbos, Journal of Luminescence 104 (2003) 239-260

[44] R. B. Jabbarov, C. Charter, B. G. Tagiev, O. B. Tagiev, N. N. Musayeva, C. Barthou, P. Benalloul, Journal of Physics and Chemistry of Solids 66 (2003) 1049-1056

[45] C. Chartier, C. Barthou, P. Benalloul, J.M. Frigerio, Journal of Luminescence 111 (2005) 147-158

[46] Y. V. Orloskii et al. Optical Materials 29 (2007) 1115-1128

[47] K. Tanaka, Y. Inoue, S. Okamoto, K. Kobayashi, K. Takizawa, Jpn. J. Appl. Phys.: vol 36 (1197) 3517-3521

[48] F.-L. Zhang, S. Yang, C. Stoffers, J. Penczek, P. N. Yocom, D. Zaremba, B. K. Wagner, C. J. Summers, Applied Physics Letters Vol 72 n° 18 (1998) pp. 2226-2228

[49] J. Zhang, M. Takahashi, Y. Tokuda, T. Yoko, Journal of The Ceramic Society of Japan 112 (9) 511-513 (2004)

[50] Scott D. Setzler, Peter G. Schunemann, Thomas M. Pollak, United States Patent 6714578

[51] C. Komatsu-Hidaka, T. Takizawa, Journal of Crystal Growth 222 (2001) 574-578

[51] F. Nakano, N. Uekura, Y. Nakanishi, Y. Hatanaka, G. Shimaoka, Applied Surface Science 121/122 (1997) 169-162

[52] M. Ishigawa, T. Nakayama, Phys. Stat. Sol. C vol 1 issue 4 pp823-826 (2004

[53] S. Nomura, T. Takizawa, S. Endo, Journal of Chemistry and Physics of Solids 66 (2005) 2090-2093

[54] H. Najafov, A. Kato, H. Toyota, K. Iwai, A. Bayramov, S. Iida, Jpn. J. Appl. Phys.: vol 41 (2002) pp. 2058-2065

[55] P. Dorenbos, Journal of The Electrochemical Society 152 (7) H107-H110 (2005)

[56] C. Guo, Q. Tang, C. Zhang, D. Huang, Q. Su, Journal of Luminescence 126 (2007), 333-338

[57] in press C. Guo et al. Mater. Res. Bull. (2007), doi:10.106/j.matteresbull.2007.02.023

Chapter 2: Optical Properties of Rare Earths doped Materials

2.1 Energy Levels of Optically Active Centres in Solids

Optically active centres are dopant ions intentionally introduced in a crystal during the growth process, or lattice defects (colour centres) created by various methods, that provide energy levels within the energy gap of the material and therefore can originate optical transitions at frequencies lower than that of the crystal fundamental absorption edge [1]. Lanthanide ions and transition metal ions are common optically active centres in solid state laser technology for the realization of active media [2].

For an isolated free ion the energy states are characterized by the total angular momentum J and, due to spherical symmetry, are $2J+1$–fold degenerate [3]. As a general rule, the active ions substitute a specific cation of the host matrix and are co-ordinated with ligand ions arranged in a specific symmetry [4]. Then the spatial degeneracy of the J states is partially or completely removed because of the lower degree of symmetry [2]. The main problem, both from the experimental and theoretical point of view, is the determination of the energy eigenvalue spectrum of the active ion within the host matrix. When the active ion is placed in a crystal lattice, it is subjected to a number of forces of very complex nature [2]. Provided that the active ion is considered to be in a static electric field generated by the neighbouring ions (named the *crystal field*), and that dynamic interactions with the lattice are neglected, an effective potential V_c can be defined [2, 1]. From a general point of view the problem can be regarded as a kind of Stark effect. The Hamiltonian for the active ion in the crystal site can be written as [4]:

$$\begin{aligned} H &= \left(-\frac{\hbar^2}{2m}\sum_i \nabla_i^2 - \sum_i \frac{Ze^2}{r_i} \right) + \sum_{j>i} \frac{e^2}{r_{ij}} + \sum_i \xi_i \mathbf{L}\cdot\mathbf{S} + \sum_i eV_c\left(r_i, \vartheta_i, \varphi_i\right) = \\ &= H_0 + H_e + H_{SO} + H_{CF} \end{aligned} \tag{2.1}$$

where the first two terms are the kinetic and potential energy of each electron in the nucleus field (H_0) and correspond to the unperturbed Hamiltonian. The remaining three terms are the Coulomb repulsive interaction between electrons (H_e), the spin-orbit interaction (H_{SO}) and the interaction between electrons and the crystal field (H_{CF}), and are treated as successive perturbations [4]. Depending on the relative strength of the crystal field, the following approximations hold [1,4,5]:

1. *Weak Crystal Field*: the magnitude of the crystal field interaction is small compared to the Coulomb electron-electron interaction and to the spin-orbit interaction ($H_{CF}<H_e,H_{SO}$) [1]. In this case the free-ion multiplets described by the quantum numbers L, S, J and M_J, are taken as the basis functions for the zero-order approximation [5]. As a result of the crystal field perturbation the $\left|L,S,J,M_J\right\rangle$ states of the

free ion are slightly shifted and split [1, 4]. Weak crystal field approximation generally holds for trivalent lanthanides, since the $4f$ electrons are shielded by the outer $5s^2\,5p^6$ electrons [4, 1];

2. *Medium Crystal Field*: the magnitude of the crystal filed is smaller than the Coulomb electron-electron interaction but larger than the spin-orbit coupling ($H_{SO} < H_{CF} < H_e$). In this case the eigenfunctions of the unperturbed system are the LS spin-orbit coupled terms of the free ion, described by the quantum numbers L, S, M_L and M_S [5]. Due to crystal field perturbation the LS coupling breaks and the free ion energy levels split. Spin-orbit coupling is then treated as an additional perturbation that further splits the energy levels. The medium crystal field approximation generally holds for first-row transition-metal ions with $3d$ unshielded electrons [4,5,1];
3. *Strong Crystal Field*: the magnitude of the crystal field is large compared both to Coulomb interaction between electrons and spin-orbit interaction (H_{SO}, $H_e < H_{CF}$). In this approximation the eigenfunctions of the unperturbed system are the single electron wave functions described by the quantum numbers l, m_l, s and m_s. The Stark levels are then found by diagonalization of H_{CF} in the $\left|l, m_l\right\rangle$ basis. Once the crystal field splitting is determined, multi-electrons crystal field terms are constructed taking into account multi-electrons Coulomb interactions. Finally, the spin-orbit interaction is treated as a successive perturbation to determine the crystal field multiplets. The strong crystal field approximation

applies to second- and third-row transition-metal ions with 4*d* or 5*d* optically active electrons [1, 4, 5].

Since the electronic wave functions are expressed in terms of spherical harmonics, it is convenient to expand the crystal field potential V_c as a linear combination of spherical harmonics [4]:

$$V_c = \sum_j \sum_l \sum_m A_{lm} Y_l^m \left(\vartheta_j, \varphi_j\right) R_l \left(r_j\right) \quad (2.2)$$

where the subscript j designates the optically active electrons and A_{lm} are the expansion coefficients that depend on the actual local environment surrounding the optically active centres [4]. Indeed the crystal field operator must transform as the totally symmetric representation of the ion-ligand cluster, in order to leave the total Hamiltonian invariant under all symmetry operation of the system [4]. Moreover, symmetry considerations allow to overcome quantum mechanical calculation in determining the number of Stark components of the activator in a given crystal [1]. It can be shown by the methods of Group Theory that the number of Stark levels in crystal fields of various symmetries depends on quantum number l (Strong Crystal Field), L (Medium Crystal Field) and J (Weak Crystal Field). In Table I the expected number of Stark components for a given activator site symmetry are reported for integer (0-8) and half-integer J values (1/2-17/2) [5].

Local Symmetry	Point Group	J=0	1	2	3	4	5	6	7	8
		2J+1=1	3	5	7	9	11	13	15	17
Cubic	O_h, T_d, O, T_h, T	1	1	2	3	4	4	6	6	7
Hexagonal	D_{6h}, D_{3h}, C_{6v}, D_6, C_{6h}, C_{3h}, C_6	1	2	3	5	6	7	9	10	11
Trigonal	D_{3d}, C_{3v}, D_3, C_{3i}, C_3	1	2	3	5	6	7	9	10	11
Tetragonal	D_{4h}, D_{2d}, C_{4v}, D_4, C_{4h}, S_4, C_4	1	2	4	5	7	8	10	11	13
Orthorhombic	D_{2h}, C_{2v}, D_2	1	3	5	7	9	11	13	15	17
Monoclinic	C_{2h}, C_s, C_2	1	3	5	7	9	11	13	15	17
Triclinic	C_i, C_1	1	3	5	7	9	11	13	15	17
		J=1/2	3/2	5/2	7/2	9/2	11/2	13/2	15/2	17/2
		2J+1=2	4	6	8	10	12	14	16	18
Cubic	O_h, T_d, O, T_h, T	1	1	2	3	3	4	5	5	6
Other lower symmetry types		1	2	3	4	5	6	7	8	9

Table I: splitting of REE^{3+} manifolds in crystal fields of given symmetry (after Kaminskii, ref [5])

As previously discussed the weak crystal field approximation generally holds for trivalent lanthanides. Indeed the $4f$ electrons are shielded by the outer $5s^2$ $5p^6$ electrons and are slightly affected by local environment. This implies that the main spectroscopic features of a trivalent lanthanide in a solid host are similar from one crystal to an other [1]. In 1968 Dieke and co-worker performed systematic spectral measurements of all the trivalent lanthanide in $LaCl_3$ [2]. This work leaded to a scheme of the $^{2S+1}L_J$ levels in $LaCl_3$ known as the *Dieke Diagram* [1, 2] Nowadays the interpretation of the spectra of trivalent lanthanide doped material is often achieved by comparison with the Dieke Diagram [1], which allows to roughly predict the wavelength of a given transition [1]. The Dieke Diagram is shown in figure 1.

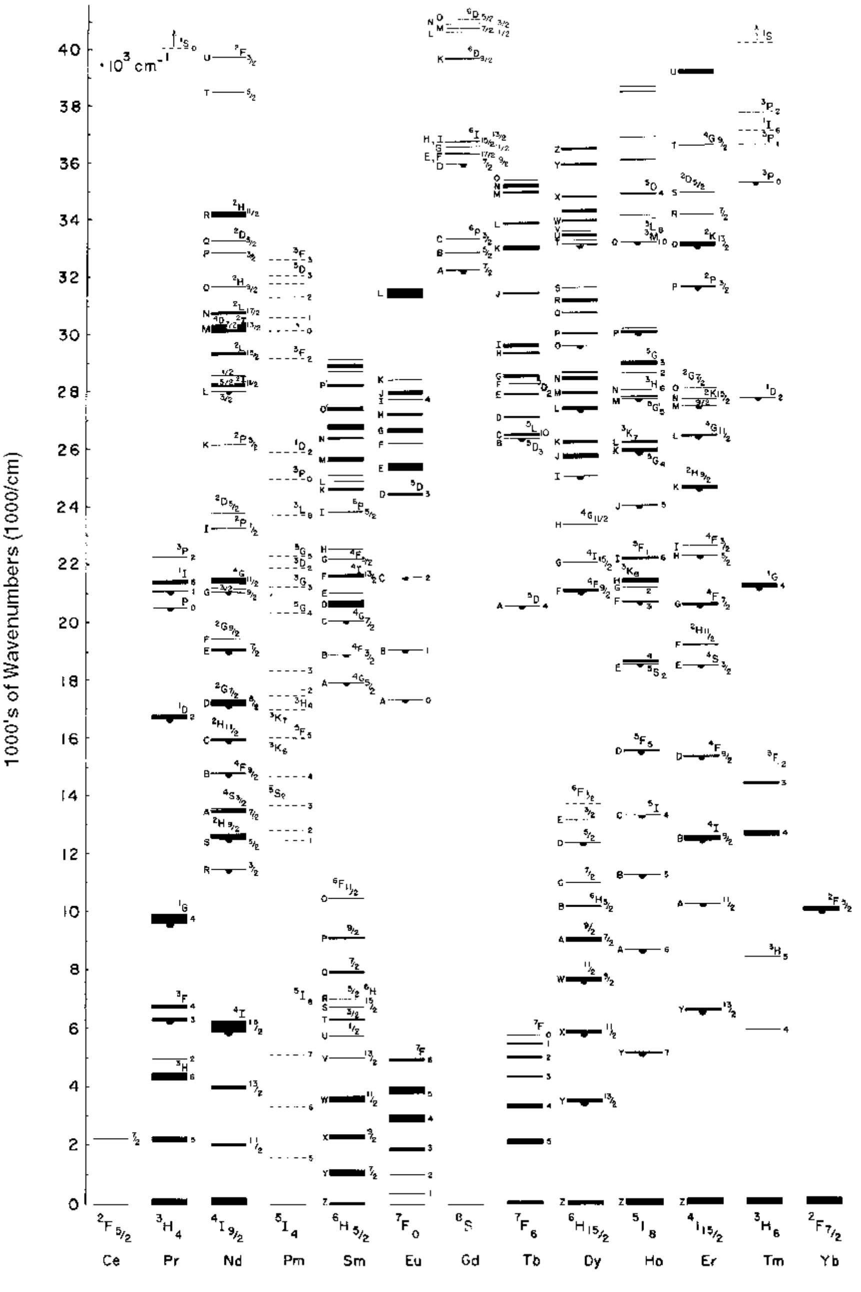

Figure 1: the Dieke Diagram

2.2 Optical Transition Selection Rules

According to Fermi's Golden Rule, the probability of transition per unit time between two non degenerate states induced by a photon of energy $h\nu$ is given by [6]:

$$W_{if} = \frac{2\pi}{\hbar} \left| \langle f | H | i \rangle \right|^2 \delta\left(E_f - E_i - h\nu\right) \quad (2.3)$$

where $|i\rangle$ and $|f\rangle$ are the initial and final state with energy E_i and E_f respectively, H is the interaction Hamiltonian between the photon and the system and the Dirac Delta function δ states the energy conservation. Optical properties of rare earth active centres are generally ascribed to electric dipole, electric quadrupole and magnetic dipole transitions [5] between Stark levels that, depending of the crystal field symmetry, are characterized by some degree of degeneracy [1,5]. Therefore the Einstein coefficients of stimulated emission, absorption and spontaneous emission are respectively [5,6]:

$$\begin{aligned} B_{ji} &= \frac{1}{g_j} \frac{8\pi^3}{3h^2} S_{ji} \\ B_{ij} &= \frac{1}{g_i} \frac{8\pi^3}{3h^2} S_{ij} \qquad (2.4) \\ A_{ji} &= \frac{1}{g_j} \frac{64\pi^4 \nu_{ji}^3}{3hc^3} S_{ji} \end{aligned}$$

where g is the degeneracy of the initial state, ν_{ji} is the frequency of the emitted photon and S_{ji} is the so called *line strength* [5]:

$$s_{ji} = \sum_{ji} \left| \langle j | M | i \rangle \right|^2 = \sum_{ji} \left| M_{ji} \right|^2 \quad (2.5)$$

where M is the electric or magnetic momentum. Thus the only quantities in Einstein coefficients that depend on crystal properties are the electric and magnetic momenta [5]. Instead of performing a detailed evaluation of the M_{ji} matrix elements, it is sometimes sufficient to determine whether they are zero or nonzero [4]. Transitions with $\left| M_{ji} \right|^2 \neq 0$ are called *allowed transitions*, while transitions with $\left| M_{ji} \right|^2 = 0$ are called *forbidden transitions* [1]. Allowed electric dipole transitions require that the initial and final states have opposite parity [1, 2]. According to this parity selection rule, transitions between $4f^n$ and $4f^{n-1}5d$ states of trivalent and divalent lanthanides are allowed [2], and give rise to intense absorption and fluorescence bands [7, 1], as in the case of Ce^{3+} and Eu^{2+} doped materials [7, 1].

For free lanthanide ions, electric dipole transitions between states of the $4f^n$ configuration are parity forbidden [2]. If the lanthanide ion is placed in a non centrally symmetric crystal lattice, the f states are admixed with state of opposite parity by crystal field interactions [2, 5]. As a result radiative transitions become *weakly* allowed at electric dipole order, and are called *forced electric dipole* transitions [8]. Forced electric dipole transitions are much weaker than ordinary electric dipole transitions [7], but the majority of radiative transitions in rare earth doped materials are ascribed to *f-f* intra-configuration transitions [2].

The two states involved in forced electric dipole transitions can be represented as a linear combination of the wave function of the ground $4f^n$ configuration $\left|4f^n\psi JJ_z\right\rangle$ with the wave function of excited $\left|\beta\right\rangle$ configurations of the opposite parity [5]:

$$\begin{aligned}\left\langle A\right| &= \left\langle 4f^n\psi JJ_z\right| - \sum_\beta \frac{\left\langle 4f^n\psi JJ_z\right|V_{CF}^{odd}\left|\beta\right\rangle\left\langle\beta\right|}{E\left(4f^n\psi JJ_z\right)-E\left(\beta\right)} \\ \left|B\right\rangle &= \left|4f^n\psi' J' J'_z\right\rangle - \sum_\beta \frac{\left|\beta\right\rangle\left\langle\beta\right|V_{CF}^{odd}\left|4f^n\psi' J' J'_z\right\rangle}{E\left(4f^n\psi' J' J'_z\right)-E\left(\beta\right)}\end{aligned} \qquad (2.6)$$

where V_{CF}^{odd} are the odd terms in the crystal field potential expansion for non centrally symmetric centres and the terms in denominators are the energies of the ground and excited states [5]. The operator of the electric dipole momentum *P* can be expanded in the *x*, *y* and *z* components of $\left(P_q^{(1)}\right)$, which induce transitions of various polarizations. In particular for $q=0$ π-polarization occurs (*z* component), while for $q=\pm1$ σ-polarization occurs (*x*, *y* components) [5]. Non zero matrix elements of the $P_q^{(1)}$ operator relate states of opposite parity admixed to $\left\langle A\right|$ and $\left|B\right\rangle$ [5]:

$$\begin{aligned}\langle A|P_q^1|B\rangle = &-\sum_{\beta}\frac{\langle\psi JJ_z|V_{CF}^{odd}|\beta\rangle\langle\beta|P_q^1|\psi' J' J'_z\rangle}{E\left(4f^n\psi JJ_z\right)-E\left(\beta\right)}\\ &-\sum_{\beta}\frac{\langle\psi JJ_z|P_q^1|\beta\rangle\langle\beta|V_{CF}^{odd}|\psi' J' J'_z\rangle}{E\left(4f^n\psi' J' J'_z\right)-E\left(\beta\right)}\end{aligned} \qquad (2.7)$$

where the sum is over all the $|\beta\rangle$ components of opposite parity. A detailed calculation of (2.7) requires not only the knowledge of the energies of the excited states but also the knowledge of V_{CF}^{odd} [5]. To overcome these difficulties the quantities $E\left(4f^n\psi JJ_z\right)-E\left(\beta\right)$ and $E\left(4f^n\psi' J' J'_z\right)-E\left(\beta\right)$ are treated as a constant ΔE independent of ψ, J and β, which is equivalent to the assumption that the electron configuration splitting is negligible compared to the energy gap between the levels [5]. This is the so called Judd-Ofelt approximation and leads to the ensuing expression for the P matrix elements [5,1]:

$$\langle A|P_q^1|B\rangle = \sum_{t.m} Y\left(t,m,q\right)\cdot\left\langle 4f^n\psi JJ_z\left|U_{m+q}^{(t)}\right|4f^n\psi' J' J'_z\right\rangle \qquad (2.8)$$

where t is an even number, the braket is the matrix element of the *(m+q)*th component of the irreducible tensor operator of rank t and $Y\left(t,m,q\right)$ a constant defined as [5]:

$$Y\left(t,m,q\right)=\sum_{k}\left(-1\right)^{m+q}\left(2t+1\right)^{1/2}A_{km}\begin{pmatrix}1 & t & k\\ q & -\left(m+q\right) & m\end{pmatrix}Z\left(k,t\right) \qquad (2.9)$$

where $Z(k,t)$ is the value proportional to the overlap integral of the radial parts of the wave functions for states belonging to the ground and excited electron configurations of the opposite parity, and inversely proportional to the energy gap therein; A_{km} is the odd parameter of the crystal field potential ($k \leq 7$) [5]. The sum of equation (2.8) over all the J_z values of the initial and final states will remove the anisotropy associated with polarization and allows to calculate the probabilities for inter-multiplets transitions [5]. Thus the line strength of force electric dipole transition is [5]:

$$S_{fed}(\psi J;\psi' J') = \frac{1}{e^2} \sum_{J_z J'_z} \left| \langle A | P_q^1 | B \rangle \right|^2 = \sum_{t=2,4,6} \Omega_t \langle \psi J J_z | U^{(t)} | \psi' J' J'_z \rangle \quad (2.10)$$

where Ω_t are the so called Judd-Ofelt intensity parameters [2]. The intensity parameters can be obtained by absorption coefficient measurements provided that the ion concentration and the refractive index of the host are known [5]. The main advantage of Judd-Ofelt formalism is that once the Ω_t are known, the line strength for any given transition between any pair of J states can be determined [1].

2.3 Optical Transition Linewidth

Several mechanisms participate to determine the linewidth $\Delta\nu$ and the line profile $g(\nu)$ of absorption and fluorescence of optically active centres [1]. Generally, a distinction is made between *homogeneous* and *inhomogeneous* mechanisms [9]. A line broadening mechanism will be called homogeneous when it broadens the line of each individual atom, and therefore of the whole system, in the same way [9]. Conversely, a line broadening mechanism will be called inhomogeneous when it distributes the resonance frequencies of the atoms over a given band and therefore gives a broadened line for the system as a whole without broadening the line of individual atoms [9]. The physical process that causes the homogeneous broadening interests each atom of the system with the same probability and therefore will give rise to a line profile described by the Lorentzian function [4]:

$$g(\nu) = \frac{\Delta\nu / 2\pi}{(\nu - \nu_0)^2 + \left(\Delta\nu / 2\right)^2} \qquad (2.11)$$

On the contrary, the physical process that causes the inhomogeneous broadening has a random distribution of occurrence for each atom, thus determining a line shape described by the Gaussian function [4]:

$$g(\nu)=\frac{2}{\Delta\nu}\left(\frac{\ln 2}{\pi}\right)^{\frac{1}{2}} e^{-\ln 2\cdot\left(\frac{\nu-\nu_0}{\Delta\nu/2}\right)^2} \qquad (2.12)$$

Inhomogeneous broadening in solids typically occurs as a result of non-equivalent static distortions in the crystalline environment of the optically active centres [1], while homogeneous broadening is related to processes that shorten the lifetime of the energy levels involved in the transition [4]. An important homogeneous broadening mechanism is due the dynamic interactions between the optical active centres and the lattice vibrations [1]. Taking into account the lattice vibrations, the Hamiltonian for the optically active centres assumes the form [1]:

$$H = H_{ion} + H_{CF} + H_L \qquad (2.13)$$

where $H_{ion} = H_0 + H_e + H_{SO}$, H_L is the lattice Hamiltonian and $H_{CF} = H_{CF}(r_i, R_l)$ is the crystalline field Hamiltonian which now depends on both the active ion electron coordinates r_i and the coordinates of the ligand ions R_l. Consequently the crystalline field couples the electronic and ion motion and the eigenfunctions are now functions of both of r_i and R_l: $\Psi = \Psi(r_i, R_l)$ [1]. In the adiabatic approximation the nuclear and electronic motions can be solved separately and the eigenfunctions can be factored as follows [10] :

$$\Psi = \psi(r_i, R_l)\chi(R_l) \qquad (2.14)$$

where $\psi(r_i, R_l)$ are the electronic eigenfuctions at the coordinates R_l and $\chi(R_l)$ are the vibrational wavefunctions. By considering just one mode of vibration and assuming the configuration coordinates q, the eigenfuction can be written as [10]:

$$\Psi = \psi(r_i, q)\chi(q) \qquad (2.15)$$

Quantum mechanical calculations lead to potential energy curves of the kind depicted in figure 2 as a function of the configurational coordinates (nuclear coordinates) [1].

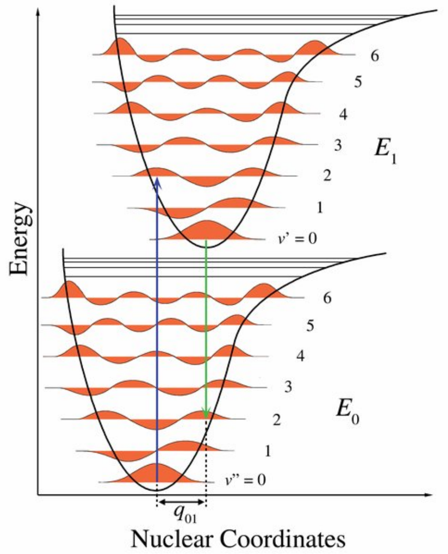

Figure 2: energy diagram as a function of configurational coordinates.

These curves represent the inter-ionic potential energy (the Morse potential) while the horizontal lines are the energy levels and the wavefunctions of lattice vibrations [1]. It is worth noting that the equilibrium coordinates for the ground and the excited state are different and that for q values close to the equilibrium position, the inter-ionic potential can be approximated by parabolas according to the harmonic oscillator approximation [1]. Therefore the inter-ionic potential energy of the ground and excited state are given respectively by [1]:

$$\begin{aligned} E_i(q) &= E_i + \frac{1}{2}\mu\omega_i^2 (q - q_0)^2 \\ E_f(q) &= E_f + \frac{1}{2}\mu\omega_f^2 \left(q - q_0^{'}\right)^2 \end{aligned} \qquad (2.16)$$

where E_i and E_f are the electronic energy eigenvalues for the ground and excited state respectively, μ is the effective mass of the oscillator and ω_i and ω_f are the characteristic angular frequencies of the ground and excited state respectively [1]. Let us recall that the energy eigenvalues of the quantum mechanical harmonic oscillator are [10]:

$$E_n = \left(n + \frac{1}{2}\right)\hbar\omega \qquad (2.17)$$

where n is the vibrational quantum number which denotes the state. Transitions from a given n state of the initial level can in principle terminate in each of the m vibrational state of the final level. Transition from $n = 0$ to

$m = 0$ are called *zero phonon line* (ZPL), and are purely electronic transition with no changes in the vibrational state of the system. Thus ZPL occurs at the same wavelengths both in absorption and emission [1]. Transitions from $n = 0$ to $m \neq 0$ give rise to phonon side-bands both in absorption and emission. Moreover the emission bands occur at wavelength larger than absorption, due to the energy dissipated in phonon transitions (Stokes law) [1] .

Provided that the temperature is sufficiently low that only the n=0 vibrational state is populated, the probability of dipole transition between the two states is given by [1]:

$$\begin{aligned} P_{if}(0\rightarrow m) &\propto \left|\langle \psi_f(q)\chi_m(q)|M|\psi_i(q)\chi_0(q)\rangle\right|^2 \\ &= \left|\langle \psi_f(q)|M|\psi_i(q)\rangle\right|^2 \cdot \left|\langle \chi_m(q)|\chi_0(q)\rangle\right|^2 \end{aligned} \qquad (2.18)$$

The square module of the overlapping between the vibrational wavefunctions does not change the overall probability due to the orthonormality of the $\chi(q)$, but just modulates the band shape. It can be shown that the previous equation reduces to [1, 11]:

$$P_{if}(0\rightarrow m) \propto \left|M_{if}\right|^2 e^{-S}\frac{S^m}{m!} \qquad (2.19)$$

where *m* is the vibrational quantum number of the terminating state and *S* is the so-called *Huang-Rhys parameter*, which is a measure of the electron-phonon interaction strength and is defined as [1, 11]:

$$S\hbar\omega = \frac{1}{2}\mu\omega^2 \left(\Delta q\right)^2 \quad (2.20).$$

The Huang-Rhys parameter is related to the Stokes shift *ΔE* between absorption ad fluorescence bands [1]:

$$\Delta E = \left(2S - 1\right)\hbar\omega \quad (2.21)$$

According to the value of the *S* parameter, usually three strengths of electron-phonon coupling are defined [11]:

- $0<S<1$ *Weak Electron-Phonon Coupling*: both absorption and luminescence spectra are dominated by a sharp ZPL accompanied by weak phonon side-bands;
- $1<S<6$ *Weak Electron-Phonon Coupling*: the spectrum is characterized by the transition to the *m* states with a phonon side-band of asymmetric, non-Gaussian profile. Moreover a weak ZPL may be observed;
- $S>10$ *Strong Electron-Phonon Coupling*: no ZPL is observed and the absorption/fluorescence band has a broad, Gaussian shape due to the envelopes (without any structure) of phonon transitions.

As the temperature increases the n ≠ 0 states are progressively populated and participate to the absorption and emission processes with a progressive increase of the band line-width [1]. It can be shown that in first approximation the linewidth Γ depends on temperature as [1]:

$$\Gamma(T) = \Gamma_0 \sqrt{\coth\left(\frac{\hbar\omega}{2kT}\right)} \qquad (2.22)$$

where Γ is the linewidth at 0 K and $\hbar\omega$ is the energy of the phonon mode coupled with the optically active ion.

2.4 Energy Transfer Processes

The non-radiative multi-phonon transitions discussed in the previous paragraph compete with radiative transitions and can strongly decrease the quantum efficiency of the photoluminescence. Therefore the total decay probability, and thus the measured lifetime at a given temperature, will be given by [1]:

$$\frac{1}{\tau} = \frac{1}{\tau_0} + A_{nr} \qquad (2.23)$$

where τ_0 is the radiative lifetime of the optically active centre and A_{nr} is the probability of non-radiative transition. The quantum efficiency is given by the ratio between the probability of radiative decay and the total decay probability [1]:

$$\eta = \frac{\tau}{\tau_0} \qquad (2.23)$$

and therefore the quantum efficiency decreases with increasing probability of non-radiative phonon transitions because of the energy transferred to the lattice [1].

Other energy transfer processes can occur between optically active centres or between optically active centres and defects of the host [1]. Depending on the type of interaction involved and on the nature of the interacting centres, energy transfer processes can inhibit or enhance the luminescence properties of the material [1].

In principle, an increase in concentration of the lanthanide ions in a given material should be accompanied by an increase in the emitted light intensity, but it has been established that such behaviour occurs up to a certain critical concentration [4]. Above this critical concentration the luminescence intensity starts to decrease [4, 1]. This process is known as *concentration quenching* of the luminescence [1]. Concentration quenching occurs as a result of a very efficient energy transfer process between the luminescent centres; it starts to have significant effect at a concentration for which there is a considerable reduction in the mean distance between the interacting centres [1]. Two mechanisms are generally invoked to explain the concentration quenching: energy transfer between the lanthanide ions and defects of the host, and interactions between the lanthanide ions [1]. In the first case due to a very efficient energy transfer, excitation energy migrates to a large number of centres being finally transferred to lattice defects or impurity ions that act as energy acceptors. These acceptors can relax to their ground state by multi-phonon emission or light emission at wavelengths different from those characteristic of the lanthanides [1]. This kind of energy acceptor centres are called *killer* or *quenching traps*, and acts as energy sink within the chain transfer, thus quenching the luminescence of the lanthanide ions [1]. The second type of mechanisms is due to energy dissipation via cross relaxation by means of resonant energy transfer between two identical adjacent centres. At large concentrations new kind of centres can be formed, due to clustering of the individual ions. This lead to a rearrangements of the energy levels that can strongly affect the fluorescence properties [1].

The energy transfer mechanisms so far discussed, inhibit the luminescence properties of the material [1, 4]. However it has been observed that energy transfer can also increase light emission and lead to an effective increase of the quantum efficiency, as in the case of some co-doped materials [1, 4, 3]. In this case the excitation energy absorbed by one kind of ion, called the *sensitiser*, is transferred to a second ion, called the *activator*, which dissipates energy by means of photon emission [1, 4]. This mechanism can be represented as follows: the sensitiser ion absorbs the incoming radiation and goes into an excited state. Then it transfers its energy to the activator ion, which moves to an excited state. Finally the activator relaxes to the ground state emitting photons [1]. To allow energy transfer some interaction between the excited sensitiser and the activator is needed. Thus the energy transfer probability rate is quantified by the ensuing equation [1, 4]:

$$P = \frac{2\pi}{\hbar}\left|\left\langle \Psi_S \Psi_A^* \middle| H \middle| \Psi_S^* \Psi_A \right\rangle\right|^2 \int g_S(E)\, g_A(E)\, dE \qquad (2.24)$$

where Ψ_S and Ψ_S^* are the wavefunctions of sensitiser's ground and excited state respectively, Ψ_A and Ψ_A^* are the wavefunctions of activator's ground and excited state respectively, H is the interaction Hamiltonian and $g_S(E)$ and $g_A(E)$ are the sensitiser emission band shape and activator absorption band shape respectively [1,4]. When the energy difference between the excited and ground state of the sensitiser and the excited and ground state of the activator are equal, the process is called *resonant* energy transfer and the overlapping integral takes its maximum value [1,4]. The interaction Hamiltonian can involve different types of interactions, such as exchange interaction and/or electric/magnetic multipolar interaction [1, 4]. Regarding multipolar interaction, dipole-dipole energy transfer occurs when both sensitizer and activator transitions are of electric dipole character [1,4]. This kind of process corresponds in general to the longest range of interaction, with probability that varies as $\frac{1}{R^6}$, R being the mean separation between sensitiser and activator. It can be shown that for dipole-dipole energy transfer equation (2.24) can be written as [4]:

$$W = \frac{1}{\tau_S^0}\left(\frac{R_0}{R_{S-A}}\right)^6 \qquad (2.25)$$

where τ_S^0 is the sensitiser fluorescence lifetime, R_{S-A} is the mean separation between sensitiser and activator and R_0 is the so called critical radius (or Föster radius). The critical radius has the physical meaning of the separation between sensitizer and activator at which the energy transfer rate equals the intrinsic decay rate of the sensitizer [1,4]. It can be shown that the critical radius is given by [4]:

$$R_0^6 = \frac{3 f_A \, \mathrm{e}^2 \Omega \eta_S}{4\left(2\pi n \langle \tilde{v} \rangle\right)^4 mc^2} \qquad (2.26)$$

were f_a is the activator oscillator strength, Ω is the overlapping integral between activator absorption and sensitizer emission cross sections, η_S is the quantum yield of the sensitizer, n is the refractive index of the host, $\langle \tilde{v} \rangle$ is the average value of wave number in the overlapping range, e, m and c are electron charge, mass and speed of light respectively [4].

Whatever the particular energy transfer is, the fluorescence lifetime of the sensitiser is affected by the energy transfer, and the decay probability must be re-written as [1]:

$$\frac{1}{\tau}=\frac{1}{\tau_0}+A_{nr}+W \quad (2.27)$$

where radiative decay probability, non-radiative transitions and energy transfer are taken into account. It has been shown that for multipolar interaction, the sensitizer time decay of fluorescence intensity follows the ensuing equation [1]:

$$I(t)=I(0)\exp\left[-\frac{t}{\tau_0}-\Gamma\left(1-\frac{3}{s}\right)\frac{C}{C_0}\left(\frac{t}{\tau_0}\right)^{\frac{3}{s}}\right], \quad s=6,8,10 \quad (2.28)$$

where Γ is the gamma function, C_0 is the critical concentration of activators (related to the critical radius), C is the concentration of activators and s is a parameter given by the type of interaction (s=6 dipole-dipole; s=8 dipole-quadrupole; s=10 quadrupole-quadrupole).

Co-doping with suitable sensitisers is widely used to improve the performances of photonics materials by means of energy transfer processes. As an example, in the commercially available phosphor $Ca_5(PO_4)_3(FCl)$ co-doped with Mn^{2+} and Sb^{3+}, the sensitisers are the Sb^{3+} ions which efficiently absorb ultraviolet radiation and transfer the excitation energy to Mn^{2+} which than exhibits high efficiency luminescence [1]. An other example of great technological relevance is Nd:YAG sensitised with Cr^{3+}, which displays high pumping efficiency with flash lamps, due to the broad band absorption of Cr^{3+} [4].

In the last years many insulating and semiconducting materials activated with rare earth elements were found to exhibits phosphorescence and thermoluminescence properties, and are attracting increasing interest due to the variety of application of long lasting phosphors [12-16]. The origin of these long lasting emissions is related to an energy transfer mechanism between trapping defects and the optically active centres [12-17]. Even thought the exact nature of the transfer is still discussed, charge carriers trapped in defects of the matrix are expected to be thermally released and migrate to the lanthanide ion, where luminescence occurs [12-16]. Moreover, it was found that co-doping with two species of lanthanide ions has relevant effects on the afterglow properties of the material, and that a suitable choice of co-dopants enhances the brightness and persistence of phosphorescence [18, 19]. It was suggested that in this case one of the co-dopants acts as a trapping centre, and may allow to achieve an effective control on the long lasting emission properties [12-19].

References

[1] J. Garcia Solè, L.E. Bausà, D. Jacque *An Introduction to the Optical Spectroscopy of Inorganic Solids*, Wiley 2005

[2] G. H. Dieke *Spectra and Energy Levels of Rare Earths Ions in Crystals* Interscience Pubblishing, New York 1968

[3] W. Koechner *Solid-State Laser Engineering* 4th edition, Springer

[4] R. P. Powell *Physics of Solid-State Laser Materials,* AIP press-Springer

[5] A.A. Kaminskii, *Laser Crystals-Their Physics and Properties*, Springer-Verlag, New York (1981)

[6] M. Fox *Optical Properties of Solids*, Oxford University Press 2001

[7] *Wide-Gap Luminescent Materials: Theory and Applications*, edited by S. R. Rotman, Kluwer Academic Publishers 1997

[8] *Luminescence of Solids* edited by M. D. Lumb, Academic Press 1978

[9] O. Svelto *Principles of Lasers 2nd edition*, Plenum Press 1982

[10] N.W. Ashcroft, N.D. Mermin *Solid State Physics*, HRW, 1976

[11] NATO Science Series II, *Defects in SiO_2 and Related Dielectrics: Science and Technoligy*, edited by G. Pacchioni, L. Skuja, D. L. Griscom, Kluwer Academic Publishers 2000

[12] T. Aitasalo, A. Durygin, J. Holsa, M. Lastusaari, J. Niittykoski, A. Suchocki, Journal of Alloys and Compounds 380 (2004), 4-8

[13] F. Clabau, X. Rocquefelte, S. Jobic, P. Deniard, M.H. Whangbo, A. Garcia, T. Le Mercier, Chem. Matter. 2005, 17, 3904-3912

[14] T. Aitasalo, D. Hreniakc, J. Holsa, T. Laamanena, M. Lastusaaria, J. Niittykoskia, F. Pelle, W. Strek, Journal of Luminescence 122-123 (2007), 110-112

[15] B. Yang, P. D. Townsend, A. P. Rowlands, Phys. Rev. B 57 n°1, 178-188 (1998)

[16] M. Yamaga, Y. Masui, S. Sakuta, N. Kodama, K. Kaminaga, Phys. Rev. B 71, 205102 (2005)

[17] S.W.S. McKeever *Thermoluminescence of Solids* - Cambridge University Press 1985

[18] H. Najafov, A. Kato, H. Toyota, K. Iwai, A. Bayramov, S. Ida, Jpn. J. Appl. Phys. Vol 41 (2002) pp 2058-2065

[19] C. Guo, Q. Tang, D. Huang, C. Zhang, Q. Su, J. Phys. Chem. of Sol. 68 (2007), 217-223

Chapter 3: Experimental and Methods

3.1 Presentation of the Experimental Study

The aim of this work was the characterization of the photoluminescence properties of rare earth doped alkaline earth thiogallates. Three main issues were investigated:

- interactions between the rare earth elements (REE) and the thiogallate matrix;
- interactions between the REE and defects of the host;
- interactions between REE in codoped samples.

The study was performed by means of time resolved photoluminescence (PL) measurements, as a function of temperature and at different excitation wavelengths. Time resolved PL measurements as a function of temperature allow to characterize the PL kinetics and band shape, thus providing information about interactions between the REE and the host matrix, and to characterize the environment of the optically active centres and the nature of the electron phonon coupling. Moreover the analysis of PL decays allows to investigate interaction between REE or interaction between the optically active centres and defects of the host matrix. In particular, interactions with host defects were investigated by means of phosphorescence (PP) and thermoluminescence (TL) measurements.

3.2 Choice of The Host Matrix and Sample Growth Technique

Materials evaluated as lanthanide host for photonics applications in the visible must fulfil the following requirements: good transmission properties in the visible and high photoluminescence efficiency. Moreover chemical stability and easy growth technique are desirable. All those requirements are fulfilled by alkaline earth thiogallates. Indeed, as discussed in chapter 1, those materials have a band gap energy of ~ 4 eV with good transmission properties in the visible. The maximum phonon energy is at about 350 cm^{-1}, a value that allows high efficiency photoluminescence. Alkaline earth thiogallates can be effectively doped with lanthanide ions up to high concentrations, due to the similarities in the ionic radii of alkaline earths and lanthanides. Moreover these materials can be growth with low-cost solid state reaction techniques and due to their environmental and chemical stability, thiogallates compounds are regarded as prospective materials for technological applications.

The samples studied in this work were grown by a solid state reaction technique at the Institute of Physics of Azerbaijan Academy of Sciences. Polycrystalline samples were prepared by placing the reactants, in form of binary compounds (alkaline earth sulphide CaS and BaS, Ga_2S_3 and rare earth fluorides), in pumped out quartz ampoules ($10^{-3} \div 10^{-4}$ Pa) placed into a one zone furnace at 1400 K temperature for 10 hours. The crystals were annealed at 1200 K for 5 hours in H_2S atmosphere after the synthesis, in order to minimize the presence of sulphur vacancies. Five set of samples were grown with nominal dopant concentration as follows:

1. $CaGa_2S_4:Ce^{3+}, Pr^{3+}$ (both Ce^{3+} and Pr^{3+} at 2% atm) ;
2. $CaGa_2S_4:Eu^{2+}$ (Eu^{2+} at 2% atm) ;
3. $BaGa_2S_4:Ce^{3+}$ (Ce^{3+} at 3% atm) ;
4. $BaGa_2S_4:Ce^{3+}, Eu^{2+}$ (both Ce^{3+} and Eu^{2+} at 3% atm)

3.3 Experimental Set up

3.3.1 Overview

Figure 1 shows the scheme of the experimental set up used in this work. Excitations wavelengths were provided by the emission of an optical parametric oscillator with frequency doubler device (Spectra Physics Quanta Ray MOPO-SL), pumped by the third harmonic (355 nm) of a pulsed Nd-YAG laser (Spectra Physics QuantaRay PRO-270). In order to prevent saturation effects or damage of the samples, neutral densities were used to decrease the excitation pulse energy to ≈1 μJ/pulse. The pulse width at half maximum was 8 ns with 10 Hz repetition rate.

PL, PP and TL measurements were performed in 90° geometry, focusing the emitted light signal onto the entrance slit of a triple grating monochromator (ARC Spectra Pro 300i). The signal was detected by a gatable intensified CCD (Princeton Instruments PI-MAX). Depending on PL bands under examination different time delays from excitation pulse and time gates were used (the so called time resolved or gated technique). Measurements as a function of temperature were performed by means of a closed-cycle He cryogenerator (CTI Cryogenics) in cold finger configuration. This system enables to perform measurements in the 9-330 K temperature range.

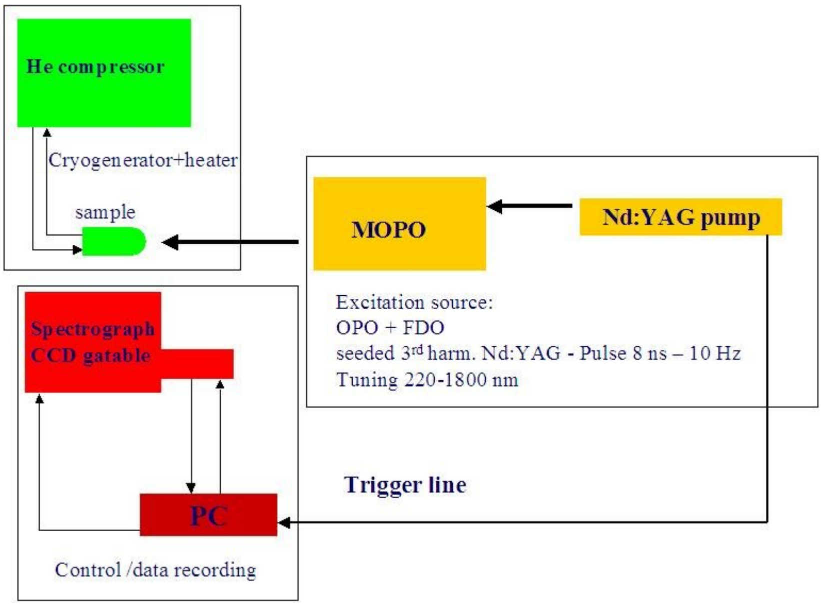

Figure 1: sketch of the experimental set up

All presented spectra are corrected for the response function of the optical system. Experimental details of specific measurements, such as excitation wavelength, emission bandwidth, gate width and time delay, are reported in the next chapters.

3.3.2 The Excitation Source

The Spectra Physics Quanta Ray MOPO-SL is an optical parametric oscillator (OPO) in master oscillator-power oscillator configuration (MOPO), pumped by the third harmonic (355 nm) of a pulsed Nd:YAG laser. The MOPO system is based on two coupled parametric oscillators, that employ two crystals of Beta Barium Borate (BBO) as nonlinear gain medium. Due to the BBO non linear polarizability, the nonlinear gain is large enough that no signal input wave is needed and the signal grows due to parametric amplification of quantum noise in the crystal. Tuning of the MOPO output is accomplished by rotating the BBO crystal with respect to the optical axis of the resonator (angle tuning). The BBO crystals for the master and power oscillators are mounted on the opposite ends of a rotary shaft, to ensure simultaneous tuning of the two cavities as the shaft rotates. In figure 2 is shown the optical scheme of the system.

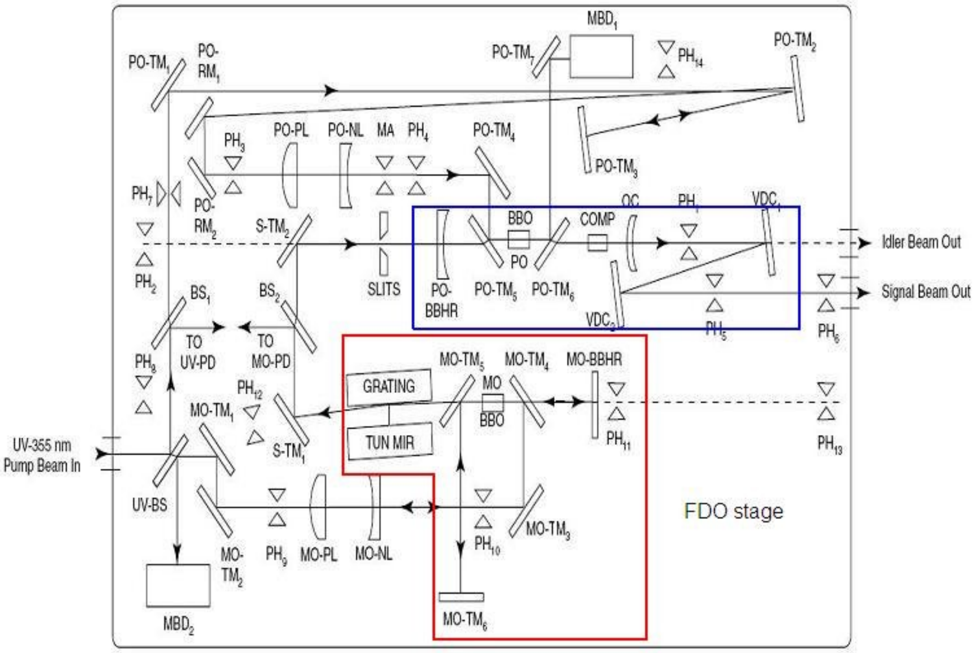

Figure 2: the MOPO-SL beam-path layout. Master oscillator and power oscillator are highlighted in red and blue respectively.

As shown in figure 2, the 355 nm pump beam is split in two beams that are separately injected into the master oscillator (MO) and power oscillator (PO) stages. When the pump pulse enters the BBO crystal in the MO (red-highlighted in fig. 2), quantum noise fluctuations result in the parametric generation of signal and idler waves. After exiting the BBO a portion of signal and idler waves deflects out of the cavity in the zeroth order (mirror) reflection, while the remaining part diffracts off the grating. As shown in figure 3, the tuning mirror is oriented to reflect back into the crystal only those signal waves with wavelengths that match the BBO gain bandwidth. After passing through the crystal, this signal waves encounter the broadband high reflector and are retro-reflected back into the cavity in the phase-matching direction.

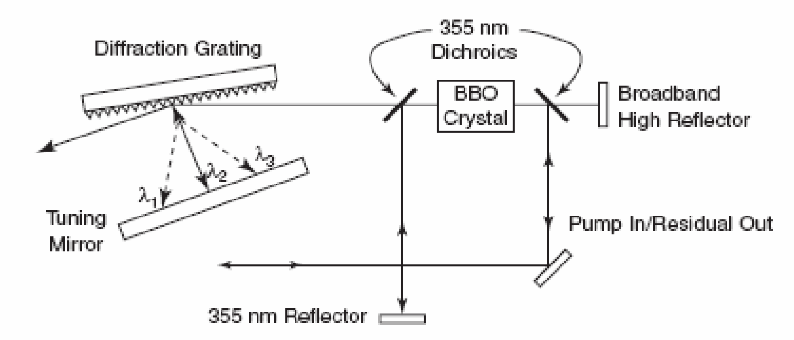

Figure 3: master oscillator optical layout

The number of signal photons in the second round trip through the cavity dominates the parametric light generated by quantum noise fluctuations. Thus, the gain realized for the spectrally narrowed signal photons dominates the gain experienced by other wavelengths. Further passes through the resonator continue to occur until the oscillation threshold is reached. Once this happens, multiple passes through the resonator result in gain depletion of the pump pulse and useful parametric output.

The MO output is obtained from the zeroth order (mirror) reflection from the diffraction grating. The beam is directed onto a routing mirror (S-TM1 in figure 2) coated with an infrared absorbing filter that removes the idler. This minimizes the chance of optical damage by reducing the total energy on the mirror. The remaining signal beam is injected into the PO (blue-highlighted in figure 2) together with the 355 nm pump beam. The optical layout of the PO is also shown in figure 4.

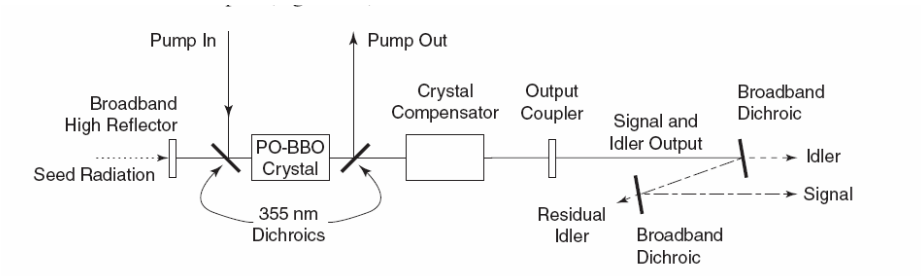

Figure 4: master oscillator optical layout

In the PO stage the signal generated in the MO are used to seed the parametric amplification, that takes fewer (with respect to MO) round trips through the cavity to reach oscillation threshold. Thus, a larger part of the pump pulse than in the MO stage is depleted and a proportional increase of the output power is realized. Collinear signal and idler are then separated by dichroic mirrors (see fig. 4) and provide coherent tunable emission from 440 nm to 1800 nm. In particular the signal wavelengths cover the range between 440 and 690 nm while the idler ones cover the range between 730 and 1800 nm. The maximum pulse energy provided by the MOPO-SL is 75 mJ at 500 nm, with a typical linewidth smaller than 0.2 cm^{-1}. Moreover a frequency doubler device (FDO-900) can be employed to further extent the MOPO-SL output from 220 to 440 nm, by means of second harmonic generation (SHG). The FDO stage optical layout is shown in figure 5.

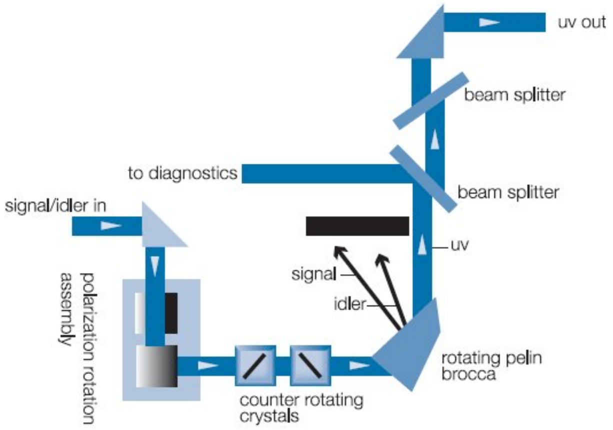

Figure 5: FDO optical layout

The FDO-900 platform is installed at the output end of the MOPO enclosure (FDO stage in fig. 2). This device employs two further BBO crystal to provide SHG over the signal and idler wavelengths. The first crystal is cut at 36° with respect to its own optical axis, while the other is cut at 56°. The first crystal realizes SHG of the idler, while the second realizes SHG of the signal. As shown in figure 5, a turning prism intercept signal and idler beams prior to being separated. Next the beam passes through a three-prism assembly where the horizontally polarized light from the MOPO is rotated of 90°. Then the beam is directed to the BBO crystals. To realize SHG one of the crystals is rotated ±15° with respect to the beam path, to set it to the proper phase-matching angle, and become the *active* crystal. The other crystal, which is not in phase-matching condition, provide compensation for beam translation and walk-off effect. After passing through BBO crystal the beam passes through a Pelin-Brocca prism which splits off the residual of signal and idler (that are directed to a beam-stop) and routes the SHG beam to the output port of the device.

3.3.3 Dispersion and Acquisition System

The ARC Spectra Pro 300i is a spectrograph/monochromator designed with Image Czerney-Turner configuration, with 300 mm of focal length and *f*-number value of 4. It employs a triple grating turret with three different gratings. The first grating is ruled with 150 G/mm with blaze wavelength at 300 nm, the second grating has 150 G/mm and blaze at 800 nm, the third grating has 600 G/mm with blaze at 500 nm. The optical layout of the system is shown if figure 6. The diverter mirror (n° 6 in fig. 6) enables the light dispersed by the grating (4) to be directed on the exit slit (8) or through the CCD port (7). The Spectra Pro 300i has a dispersion of 2.7 nm/mm with accuracy of ±0.2 nm and repeatability of ±0.05 nm (with a 1200 G/mm grating).

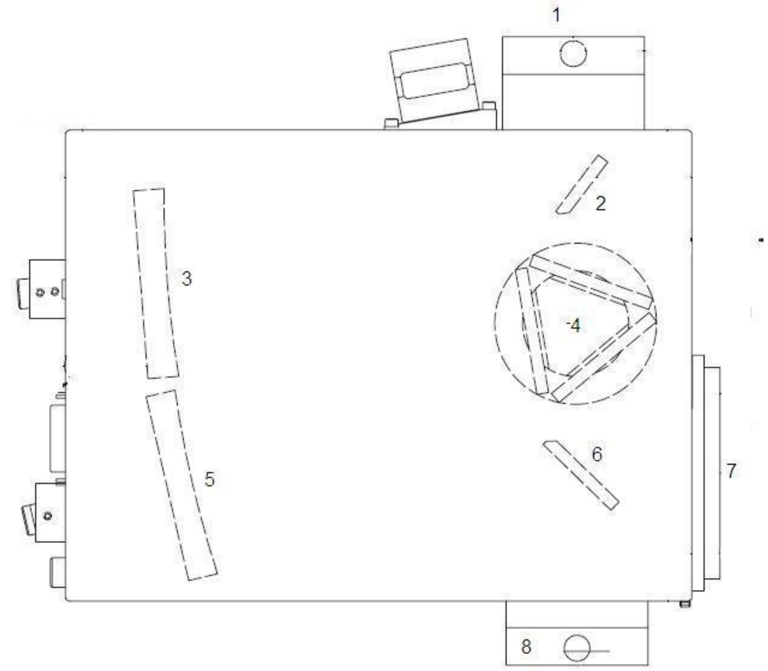

Figure 6: spectrograph optical layout

The CCD employed in this work was the PI-MAX model from Princeton Instruments. The PI-MAX is a time-gatable, image-intensified camera, with a 1024X256 pixel front illuminated CCD. In figure 7 are shown the main components of the image intensifier of the PI-MAX. Photons impinge on the photo-cathode, which has a bias of –200V, and photoelectrons are emitted. The photo-cathode is characterized by a spectral working range between 180 and 789 nm with quantum efficiency of ~ 10% (UV-visible). Photoelectrons are accelerated and amplified by passing through a micro-channel plate (MCP), which is made of silica capillaries with a metal coating on the inner surface. Thus the number of photoelectron increases due to electrons emitted from the metal after photo-electrons strike the surface.

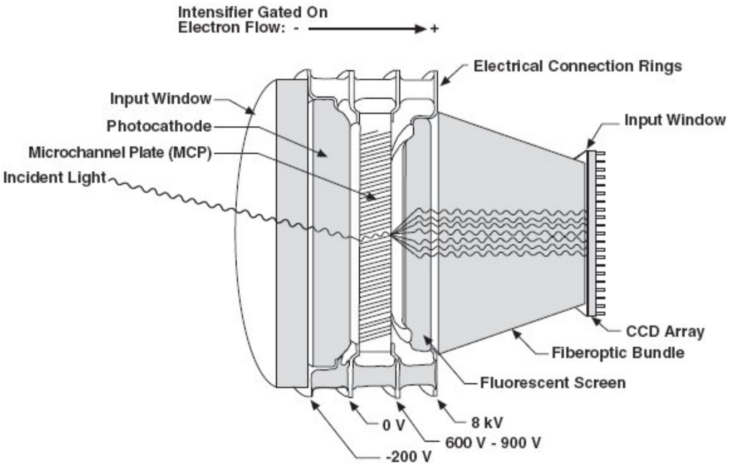

Figure 7: main components of the image intensifier

Then photoelectrons are further accelerated (8 kV) and strikes on a F43 phosphor. The light emitted from the phosphor is collected by a fiber optic bundle coupled with the CCD. Time gating and amplification of the light signal is thus achieved by applying an high voltage bias (600-900V) to the end of the MCP, with timing generated from the laser trigger source.

The PI-MAX enables gate pulse width and delay between 0 and 60s with 35 ps of resolution, with a maximum repetition rate of 250 KHz. In order to minimize the dark current, the CCD array is thermo-cooled to –20°C (with air cooling of the Peltier device).

Chapter 4:

Photoluminescence Properties of Eu^{2+} in calcium thiogallate

In this chapter experimental results on the photoluminescence properties of $CaGa_2S_4$:Eu^{2+} *are presented. Data are discussed in the framework of linear electron-phonon coupling and allowed to determine the energy of the effective phonon and the strength of the interaction.* Eu^{2+} *fluorescence lifetime was found to increase with increasing temperature. According to the Feofilov model, the lifetime temperature dependence is explained with the thermal population of a metastable state of the 4f5d manifold of Eu ions.*

4.1 Experimental details and results

Photoluminescence measurements were performed with the time resolved (gated) technique: depending on PL bands under examination different time delays from the excitation pulse and integration time (gate width) were used. Time resolved PL measurements were performed as a function of temperature from 9 K up to 325 K. Excitation was provided by the MOPO emission at 400 nm (3.1 eV) with energy of ≈1 μJ/pulse. The reported measurements were carried out with a spectral band width of 0.01 eV.

The photoluminescence spectrum recorded at 9 K is shown in figure 1. The PL emission is peaked at 2.21 eV with a full width at half maximum (FWHM) of ≈140 meV. No zero phonon line emission (ZPL) was observed.

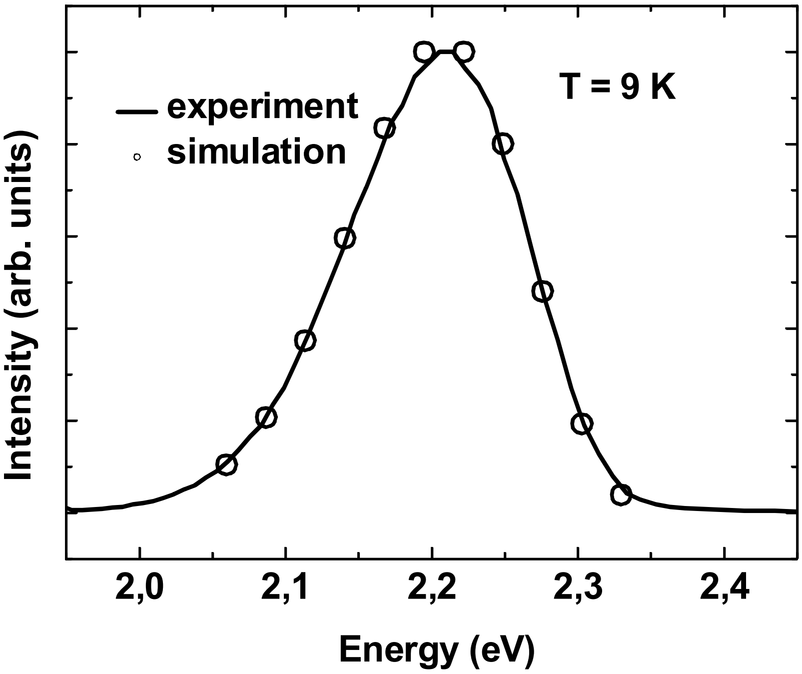

Figure 1 : time-resolved spectrum recorded at 9 K (full line) and theoretical band shape (open circles, see text for details); spectrum recorded with a gate width of 1 μs

In figure 2 PL spectra recorded at 25, 125, 210 and 290 K are shown: as temperature increases PL FWHM increases and its intensity decreases. At 325 K the PL maximum shifts to lower energy peaking at 2.19 eV with a FWHM of 190 meV.

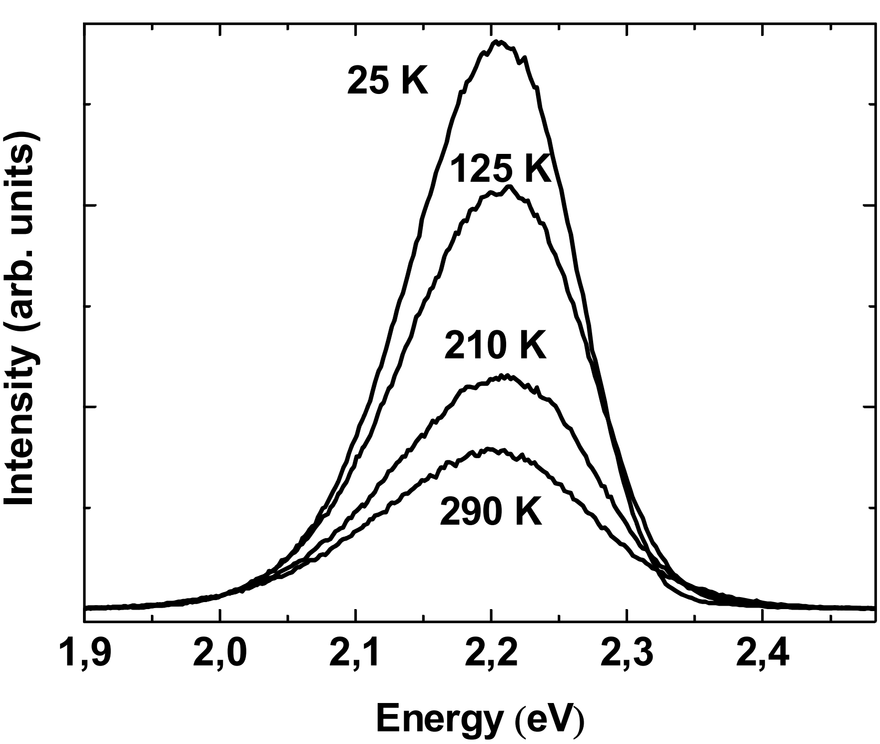

Figure 2: time-resolved spectra as a function of increasing temperature (gate width 1 μs)

In figure 3 time decays of PL at the emission peak wavelength are shown for three different temperatures. All decays are single exponentials and show that the Eu^{2+} fluorescence lifetime increases with increasing temperature. At 9 K the measured lifetime is $(453 \pm 2)ns$ and keeps constant up to 120 K; afterwards, the lifetime increases with increasing temperature and reaches the value of 599 ns at 325 K.

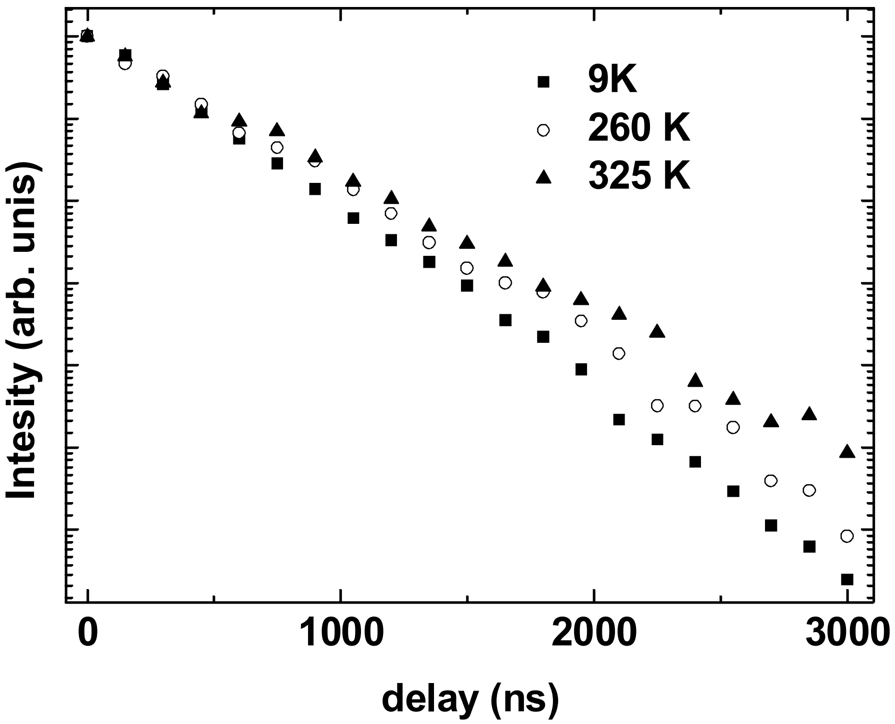

Figure 3: PL intensity decay curves as a function of temperature

4.2 Data analysis and discussion

At low temperature the lineshape of vibronic photoluminescence is described by the following equation, provided that the excited level is in its lowest vibronic state [1]:

$$I_{0\rightarrow m} \propto e^{-S}\frac{S^m}{m!} \qquad (1)$$

where *S* is the Huang-Rhys factor and *m* is the vibronic quantum number of the final state of the transition. We performed a numerical simulation of the spectrum recorded at 9K by applying eq. 1. We found that a good reproduction of experimental data (full line in fig. 1) is achieved with the following parameters: S = (5.0±0.5), zero phonon line (ZPL) at (2.33±0.02) eV and energy of effective phonon of (27±2) meV. The obtained value of the Huang-Rhys factor indicates an electron-phonon coupling of medium strength which causes the observed asymmetry of the PL band [2] and a ZPL intensity too small to be observed. The value of the energy of ZPL is in agreement with previously reported excitation of the photoluminescence spectrum (PLE) that overlaps with the emission spectrum in the region between 2.28 and 2.35 eV [3, 4]. The values of 27 meV for the phonon energy is comparable with values reported in previous works [3], taking into account that such results were achieved at higher temperature (T=77K, $\hbar\omega$=34 meV).

In figure 4 the PL band FWHMs are shown as a function of increasing temperature. At first order approximation the temperature dependence of the PL linewidth follows the ensuing equation [1]:

$$\Gamma(T) = \Gamma_0 \sqrt{\coth\left(\frac{\hbar\omega}{2kT}\right)} \qquad (2)$$

where Γ_0 is the linewidth at 0 K, $\hbar\omega$ is the effective phonon energy and k is the Boltzmann constant. As shown in fig. 4, the experimental data are in agreement with the theoretical model up to 200 K. Afterwards, the PL band broadens at a slower rate. It is worth noting that at temperatures higher than 200 K the PL emission shifts to low energy (fig. 2) and the lifetime lengthening becomes evident (fig. 3), thus indicating that the hypothesis of eq. 2 is no longer valid. Indeed eq. 2 holds provided that no variation are observed in the spectral and time decay properties of the PL [1-2].

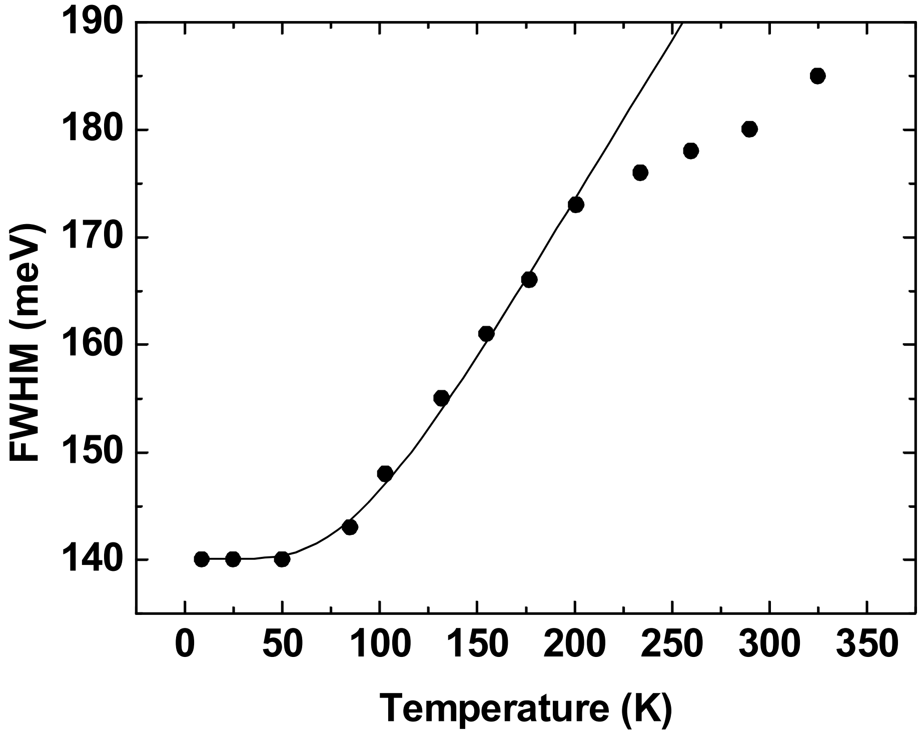

Figure 4: temperature dependence of FWHM (full circle) and best fit according to eq. 2 (full line)

According to equation 2, the best fit of experimental data between 9 and 200 K was achieved with $\Gamma_0 = 141$ meV and $\hbar\omega = 25$ meV. The very good correspondence between the value of effective phonon energy obtained by the simulation of the lineshape at 9 K and the fitting of the band thermal broadening indicates that the energy of the phonon coupled with Eu ions is ≈26 meV (210 cm^{-1}). In addition the values obtained for the Huang-Rhys factor and phonon energy allow us to estimate the Stoke shift *ΔS* as 225 meV, which predicts the absorption maximum at ≈ 2.44 eV. This value is in good agreement with previously reported measurements [3,4].

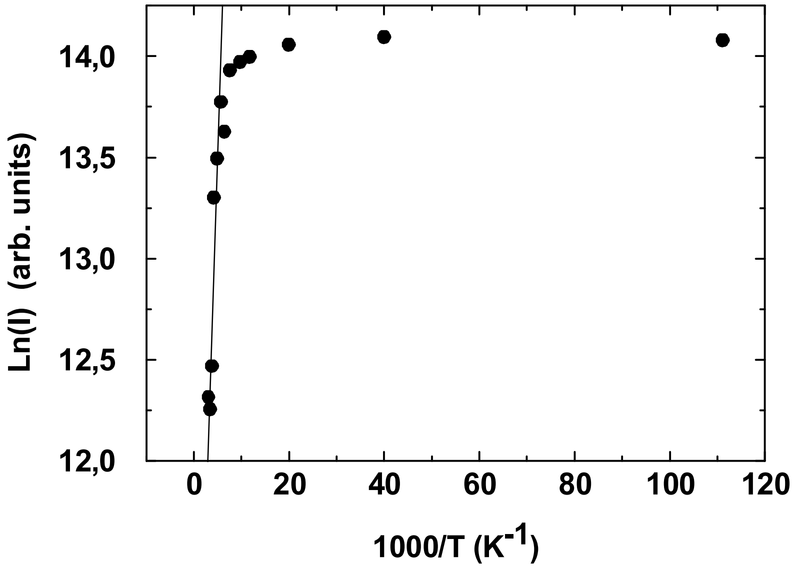

Figure 5: Arrhenius plot of the Eu emission

The Arrhenius plot of PL intensity is shown in figure 5. From linear interpolation of experimental data at higher temperatures we found an activation energy of 56 meV. It has been pointed out that the ground state of Eu^{2+} ions in calcium thiogallate should be about 200 meV from the top of valence band. Therefore the observed PL quenching may originate from a thermal excitation from the 4f5d state to an intra-gap level at about 56 meV from the Eu excited state.

In figure 6 the PL lifetimes are shown as a function of increasing temperature. From 9 K up to 150 K the lifetime remains constant while it progressively increases at higher temperatures. In conformity with previous works [5-8], we hypothesized that the lengthening of lifetime could be ascribed to thermal charging of an excited state of the 4f5d manifold with low probability of radiative decay toward the Eu ground state (Feofilov model). At low temperature the transition should originate from a level characterized by an allowed selection rule, while at higher temperatures it involves a higher energy level with a forbidden selection rule. Under this assumption the observed lifetime of the 4f5d manifold is given by [8]:

$$\tau(T) = \frac{1 + g\exp\left(-\frac{\Delta E}{kT}\right)}{R_F + R_A g\exp\left(-\frac{\Delta E}{kT}\right)} \qquad (3)$$

where R_F and R_A are the radiative decay rates of the allowed and forbidden transitions respectively. $\Delta E = E_A - E_F$ is the separation in energy between the two levels and g the ratio of their respective degeneracies.

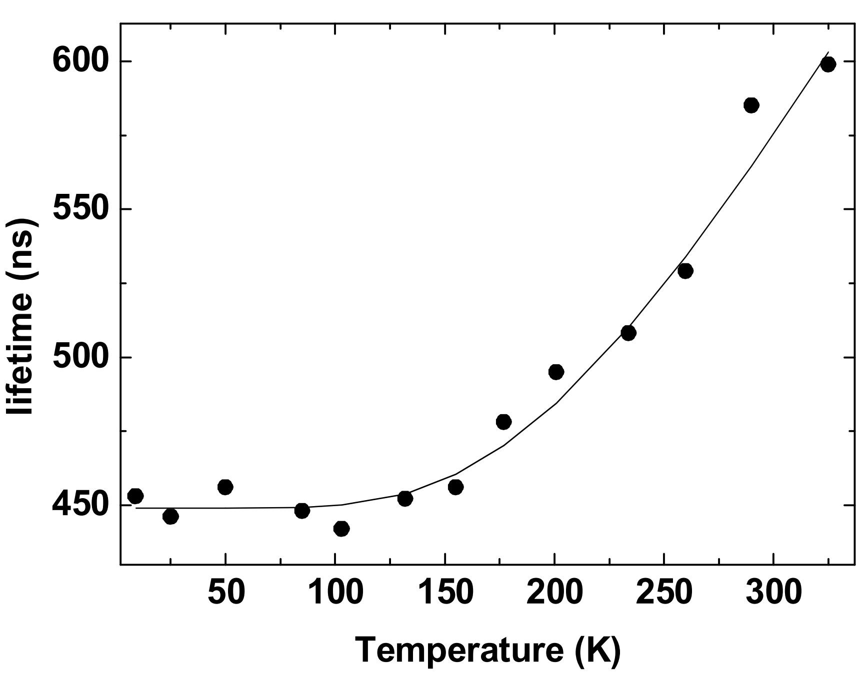

Figure 6: temperature dependence of fluorescence lifetime (full circles) and best fit according to eq. 3 (full line)

Experimental data were fitted with equation 3, thus leading to the following parameters: $R_A = 2 \cdot 10^6$ s^{-1}, $R_F = 2 \cdot 10^{-7}$ s^{-1}, $\Delta E = 67$ meV and $g = 0.27$. The value of R_A is in agreement with the expected decay rate for dipole allowed transitions, while the energy separation of 67 meV is comparable to the activation energy of the PL quenching (fig. 5). Since no slow emission was observed as the temperature increased, the following hypothesis can be advanced: at low temperature electrons are optically excited from the ground state $^8S_{7/2}$ to the lowest 4f5d level and then radiatively decay with the emission at 560 nm with a lifetime of 450 ns. With increasing temperature, electrons are thermally excited to an a higher energy level characterized by a transition rate toward the ground state of 10^{-7} s^{-1}. The *red shift* observed at 325 K may not be due to the optical transition from this excited level to ground state, therefore the red shift could be ascribed to the details of electron-phonon interactions [5]. The value of *g* found in our analysis indicates that the two levels have a relatively large degeneracy ratio. The value g = 0.27 may be related to the splitting of the 4f5d manifold in ligand environment with D_2 and C_2 symmetry.

4.3 Review of the Main Results

The photoluminescence properties of Eu-doped calcium thiogallate were studied by means of time-resolved measurements as a function of temperature. Photoluminescence properties are discussed in the framework of linear electron-phonon coupling and indicate a medium-strength interaction of the activator ions with phonons of the host matrix. The main results of the discussed analysis are summarized in table I.

Transition	Energy (eV)	FWHM (meV)	S	$\hbar\omega$ (meV)	ΔS (meV)	τ (ns)	Rate (s^{-1})
$4f^6 5d^1 \rightarrow {}^8S_{7/2}$	2.21^a	140^a	5	25	225	453^a	$2 \cdot 10^{6\,a}$
	2.19^b	190^b				599^b	

[a] T= 9 K

[b] T= 325 K

Table I: Summary of the parameters determined for Eu radiative transitions

The Eu^{2+} emission lifetime increase is explained by a thermal excitation mechanism: at low temperature the PL originates from the lowest 4f5d, while above 150 K electrons are excited to an upper level characterized by a relatively low transition rate to the ground state. This *metastable* level is located at ≈ 60 meV from the low-lying 4f5d level.

References

[1] J. Garcìa Solè, L.E. Bausà, D. Jaque, An Introduction to the Optical Spectroscopy of Inorganic Solids pp 175-180, Wiley (2005)

[2] Nato Science Series II-Defects in SiO_2 and Related Dielectrics: Science and Technology edited by G. Pacchioni, L. Skuia, D.L. Griscom, pp 74-80, Kluwer Academic Publisher (2000)

[3] S. Iida, A. Kato, M. Tanaka, H. Najafov, and H. Ikuno, J. Phys. Chem. Sol. **64**, 1815 (2003).

[4] S. Iida, T. Matsumoto, N. Mamedov, G. An, Y. Marujama, A. I. Bairamov, B. G. Tagiev, O. B. Tagiev, and R. B. Dzhabbarov, Jpn. J. Appl. Phys., Part 2 **36**, L857 (1997).

[5] J. P. Spoonhower, T. Kobayasi, S. Mrczkowski, J. F. Owen, and L. H. Brixner, J. Lumin. **21**, 247 (1980).

[6] J. P. Spoonhower and M. S. Burberry, J. Lumin. **43**, 221 (1989).

[7] A. Meijerink and G. Blasse, J. Lumin. **47**, 1 (1990).

[8] J. L. Sommerdijk, J. M.P.J. Verstegen, and A. Bril, J. Lumin. **8**, 502 (1974).

Chapter 5:

Photoluminescence Properties of Ce and Pr co-doped calcium thiogallate

In this chapter the room temperature photoluminescence properties of calcium thiogallate codoped with Ce and Pr are presented. Line shaped emissions superimposed over a wide and composed luminescence band were observed. Different components were distinguished by means of time resolved photoluminescence measurements, and were attributed to the dopant species. A band at 2.24 eV, not previously reported, was observed.

5.1 Experimental Details

Stationary photoluminescence measurements (S-PL) were performed at room temperature. Excitation was provided by a MgF_2 sealed deuterium lamp (Hamamatzu mod. L1835). Light was dispersed by a 0.3 m scanning monochromator (McPherson mod. 218). The excitation wavelength was set at 300 nm (4.1 eV) with a spectral band pass width of 5 nm. Time resolved photoluminescence measurements (TR-PL) were performed at room temperature. The excitation light was provided by the emission at 300 nm (4.1 eV) of an optical parametric amplifier (Spectra Physics OPA 200C), pumped by a pulsed Ti:saffire laser (Spectra Physics Hurricane system) with 1 KHz repetition rate. PL spectra were recorded in 90° geometry by focusing the light emission into the entrance slit of a triple grating spectrograph (ARC SpectraPro 275) and detecting the light signal with an intensified CCD detector (Princeton Instruments PI MAX). Depending on the PL bands under examination, different delays from the laser excitation were used. Spectral resolution was better than 10^{-2} eV while temporal resolution was 5 ns.

The spectra were corrected for the spectral response of the optical systems.

5.2 Results and Discussion

S-PL spectrum under 4.1 eV excitation is shown in figure 1a). Three overlapping PL bands are present, with intensity maxima at 2.64 eV and at about 2.4 and 2.2 eV. Six line shaped emissions are resolved and peaked at 1.67, 1.90, 1.96, 2.03, 2.30 and 2.51 eV, and a PL structure is observed around 1.75 eV.

Time resolved PL spectra excited at 4.1 eV, recorded at different delay time are shown in figure 1b) and 1c). Spectrum 1b) was recorded at zero delay time from the excitation pulse, with a temporal gate width of 5 ns. Compared with the S-PL spectrum, only the components at 2.42 and 2.64 eV are observed; moreover a shoulder is observed at 3 eV (on magnified intensity in fig. 1b). The emissions at 2.64 and 2.42 eV are in good agreement with those observed in previous works in $CaGa_2S_4:Ce^{3+}$ which were attributed to radiative transitions from the lowest 5d state to

$^2F_{5/2}$ and $^2F_{7/2}$ states of Ce^{3+} [1, 2, 3]. The emission at 3 eV reproduces the properties of the emission previously reported and attributed to fast radiative transition from the E_g component of the 5d state to the ground state of Ce^{3+} [2, 3]. Spectrum 1c) was recorded at 500 ns delay time from the excitation pulse with a time gate width of 500 ns. In this spectrum all the line shaped emissions observed in spectrum 1a) are present; in addition PL bands at 2.2 eV and 2.64 eV are observed. All sharp emissions shown in figure 1c) are in agreement with Pr^{3+} emissions observed in calcium thiogallate [3, 4]. Table I summarizes the energy of the lines and their attribution as reported in ref. 3 and 4. Regarding the band at 2.2 eV to our best knowledge no previous reports have been published.

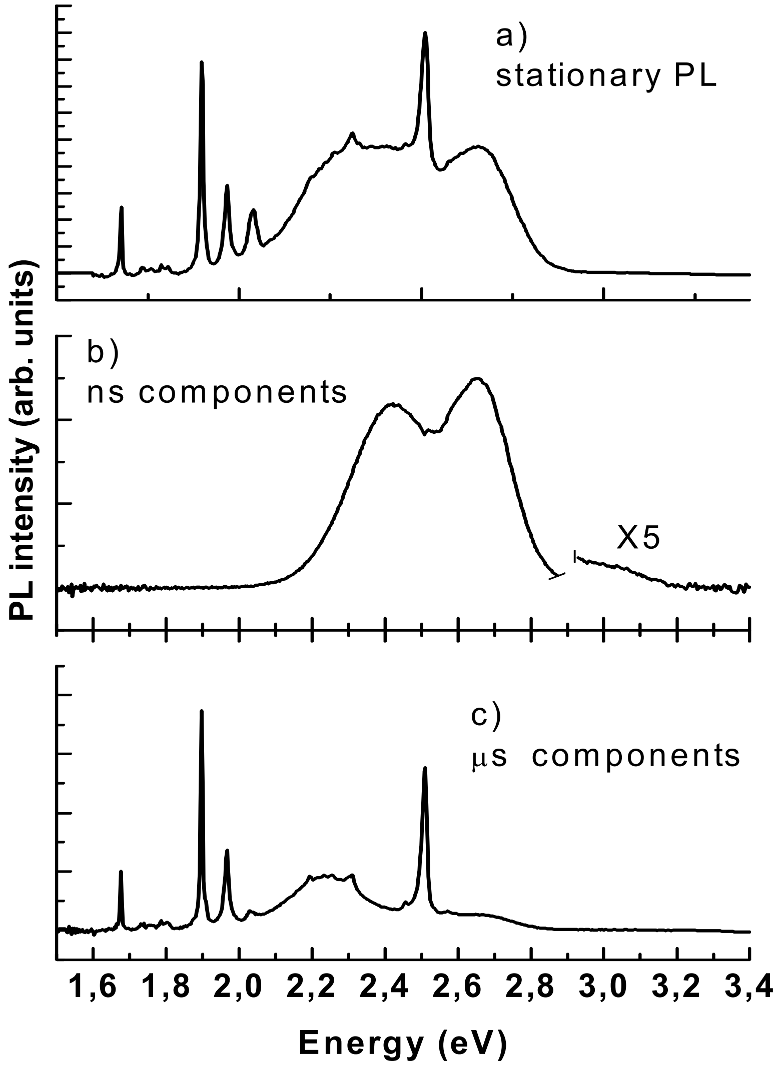

Figure 1: stationary PL spectrum (a); time resolved spectrum with zero delay time and temporal gate width of 5 ns (b); time resolved spectrum with delay time of 500 ns and temporal gate width of 500 ns (c);

Energy (eV)	**Pr^{3+} transitions**
1.67	$^3P_0 \rightarrow {}^3F_4$
1.90	$^3P_0 \rightarrow {}^3F_2$
1.96	$^3P_0 \rightarrow {}^3H_6$
2.03	$^1D_2 \rightarrow {}^3H_4$
2.30	$^3P_1 \rightarrow {}^3H_5$
2.51	$^3P_0 \rightarrow {}^3H_4$

Table I: Spectral position of line shaped emissions and attribution to Pr^{3+} transitions after ref. [3, 4]

Decay curves of the emission at 2.42, 2.64 and 3 eV are shown in figure 2 in a semi-log scale. The band at 3 eV presents a simple exponential decay with a time constant of 10 ns. This value is in very good agreement with a previous determination [3]. The bands at 2.64 and 2.42 eV show composite decay curves: up to 120 ns the two emissions intensities decrease with single exponential law with the same time decay constant of 23 ns within experimental resolution. After this initial decay, a non exponential slow tail is observed, caused by the overlapping with the slower band at 2.2 eV. It should be pointed out, anyway, that a similar non-exponential tail has been previously observed, and attributed to non radiative processes [3].

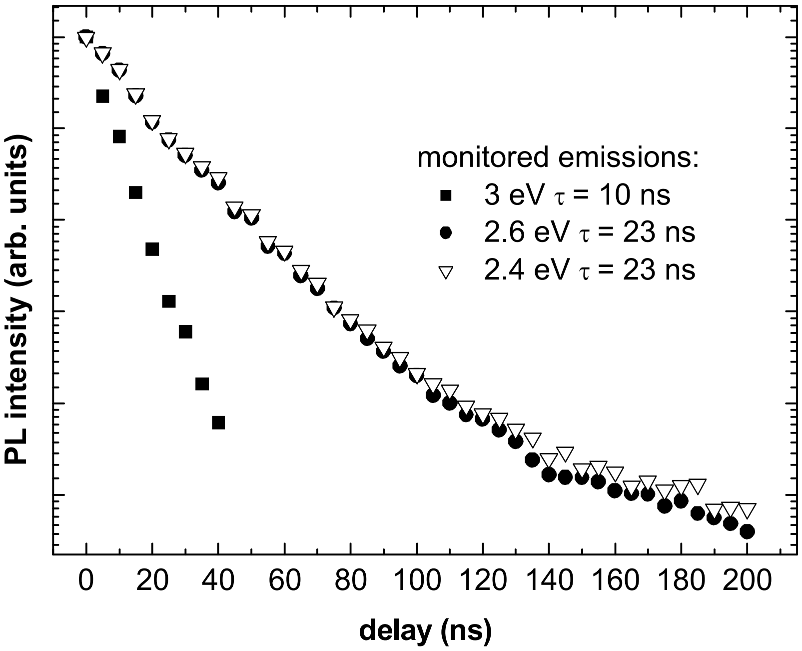

Figure 2: time decay curves of Ce^{3+} photoluminescence

Decay curves of emissions involving transitions from the $^3P_0$ and $^1D_2$ states of Pr^{3+} are shown in figure 3 in a semi-log scale. The luminescence ascribed to transitions from the $^3P_0$ state presents a single exponential decay, with time constants around 5 μs (see fig. 3 for details); the emission at 2.03 eV from $^1D_2$ to $^3H_4$ state presents a decay constant of 15 μs. The initial part of the decay curve of this emission presents a faster, non-exponential component which is due to the overlapping with the emission at 2.2 eV.

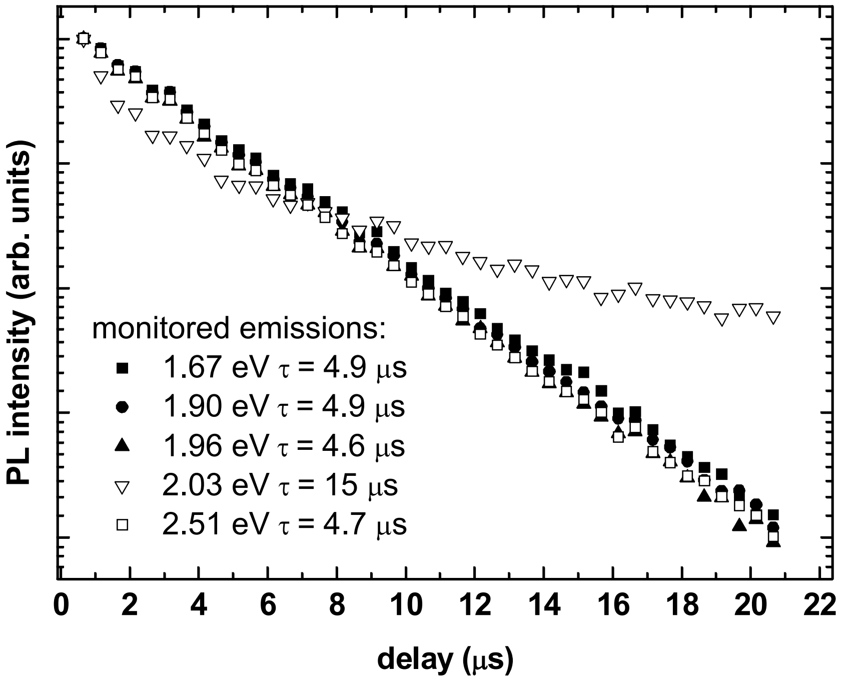

Figure 3: time decay curves of Pr^{3+} photoluminescence

The PL spectrum recorded at different delay time from the excitation pulse for the band at 2.2 eV, is shown in figure 4. As the delay increases, several peaks are resolved at 2.20, 2.23, 2.25 and 2.30 eV, superimposed over the band centred at around 2.2 eV. Peak energies are in agreement with the energies of praseodymium emissions previously observed in calcium thiogallate [2, 3]. In particular the emissions at 2.30 and 2.20 eV have been attributed to the radiative transitions from $^3P_1$ state to $^3H_5$ state and from $^3P_0$ state to $^3H_5$ state respectively [2, 3].

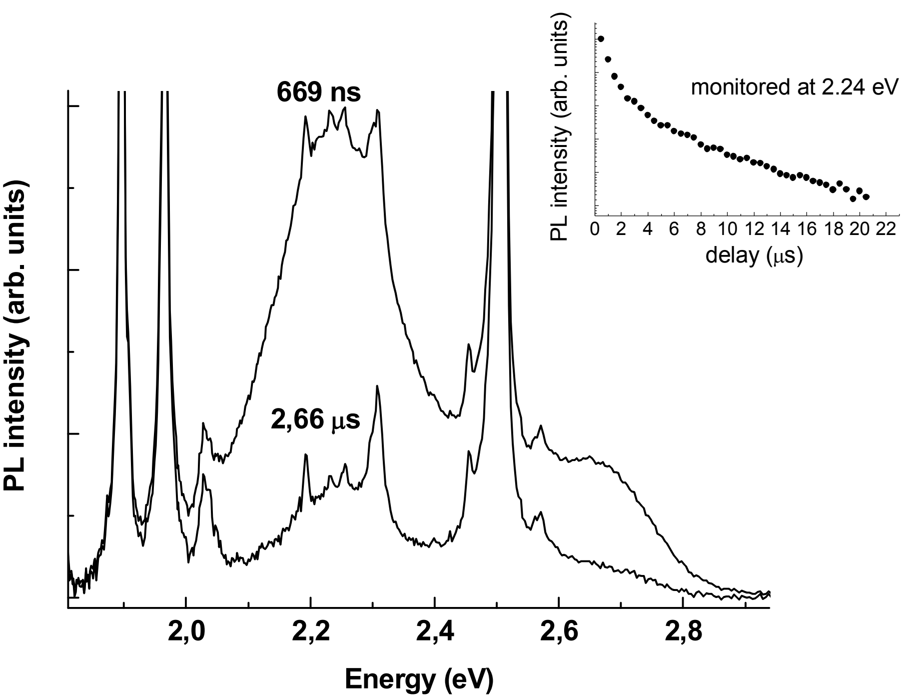

Figure 4: time resolved spectrum of the band at 2.2 eV recorded at different delay times; inset shows the decay curve

The time decay curve of PL intensity measured at 2.24 eV is shown in figure 4 in a semi-log scale. At least two components are observed which are consistent with the double nature of this band. By fitting the slow tail with an exponential decay a time constant of 5 μs is estimated, a value which is compatible with lifetime of Pr^{3+} excited states as observed in this work. For the fast component, probably due to the band at around 2.2 eV, no satisfactory exponential fit was achieved and we qualitatively estimate a decay time of 700 ns. Spectral position and decay features of the band at 2.2 eV could account for the non exponential tail observed in the decay of Ce emissions, suggesting an alternative interpretation to previously reported non radiative processes [3].

A final comment pertains the band at 2.2 eV. The collected data do not allow to identify the origin of the emission, but it could be related to defects of the thiogallate matrix. Indeed thiogallates compounds are known to be characterized by non perfect stoichiometry, interstitial or vacancies defects that often give rise to PL properties. Further measurements are in progress in order to clarify the nature of the emission at 2.2 eV

5.3 Review of Main Results

The general features of PL properties at room temperature of calcium thiogallate doped both with trivalent cerium and praseodymium were discussed for the first time. PL components arising from Ce and Pr centres have been resolved by means of time resolved spectroscopy. The PL parameters of $CaGa_2S_4$:Ce,Pr determined in this work were compared with previously published data obtained on single-doped samples. Results show that Ce and Pr properties observed in single-doped samples are preserved in the presence of co-doping suggesting that no interaction takes place between Ce and Pr.

A band at 2.2 eV has been observed for the first time, which seems to affect the time decay features of Ce PL.

References

[1] A. Bayramov, H. Najafov, A. Kato, M. Yamazaki, K. Fujiki, Md. Nazri, S. Ida - J. of Phys. Chem. Solids 64, 1821-1824 (2003)

[2] A. Kato, M. Yamazaki, H. Najafov, K. Iwai, A. Bayramov, C. Hidaka, T. Takizawa, S. Ida - J. of Phys. Chem. Solids 64, 1511-1517 (2003)

[3] A. Bessiere, P. Dorenbos, C. W. E. van Eijk, E. Yamagishi, C. Hidaka, T. Takizawa - J. of Electroc. Soc. 151 (12) H254 – H260 (2004)

[4] A. Garcia, F. Guillen, C. Fousassier - J. of Luminescence 33, 15-27 (1985)

Chapter 6:

Low Temperature Thermoluminescence in $CaGa_2S_4:Eu^{2+}$

In this chapter the phosphorescence decay and thermoluminescence properties of $CaGa_2S_4:Eu^{2+}$ *as a function of temperature are presented. The comparison between spectra recorded as a function of delay time from the excitation pulse at different temperatures indicates that long lasting emissions peaked at about 2.2 eV occur at* Eu^{2+} *sites. Experimental data are discussed in the framework of generalized order of kinetic model and allow to estimate the activation energies of the trapping defects. The observed thermoluminescence components are correlated to trapping defects induced by* Eu^{2+} *doping, and to a continuous distribution of defects.*

6.1 Experimental details

Time resolved photoluminescence (PL), phosphorescence (PP) and thermoluminescence (TL) measurements were performed as a function of temperature from 9 K up to 325 K. The sample excitation was provided by the emission at 260 nm (4.77 eV) of the MOPO with an excitation pulse energy of ≈1 μJ/pulse, the pulse width was of 8 ns with 10 Hz repetition rate. PL, PP and TL spectra were recorded with a spectral bandwidth of 0.1 eV. Depending on the PL bands under examination different time delays from excitation pulse and time gates were used. PP measurements were performed at constant temperature after excitation of the sample for 10 minutes. TL measurements were performed after irradiation of the samples for 10 minutes at 35 K. Samples were heated with a linear heating program at rate of 0.1 Ks^{-1}. The recording of the spectra was synchronized with the heating rate in order to have a resolution of 0.2 K/spectrum. If compared to thermoluminescence measurements performed with photomultiplier tubes, the use of the CCD allows to record the spectral distribution of the thermally stimulated emission at each point of the glow curve.

All spectra were corrected for the spectral response of the optical system.

6.2 Results

Time resolved PL spectra recorded at 25 K are shown in figure 1 as a function of the time delay from the excitation pulse. The characteristic Eu^{2+} radiative transition from $4f^65d^1$ state to the ground state [1-7] is observed at 2.2 eV (564 nm). By comparison between PL spectra recorded at different delays from excitation pulse, no variation in the band shape of the PL is observed with increasing delay from excitation.

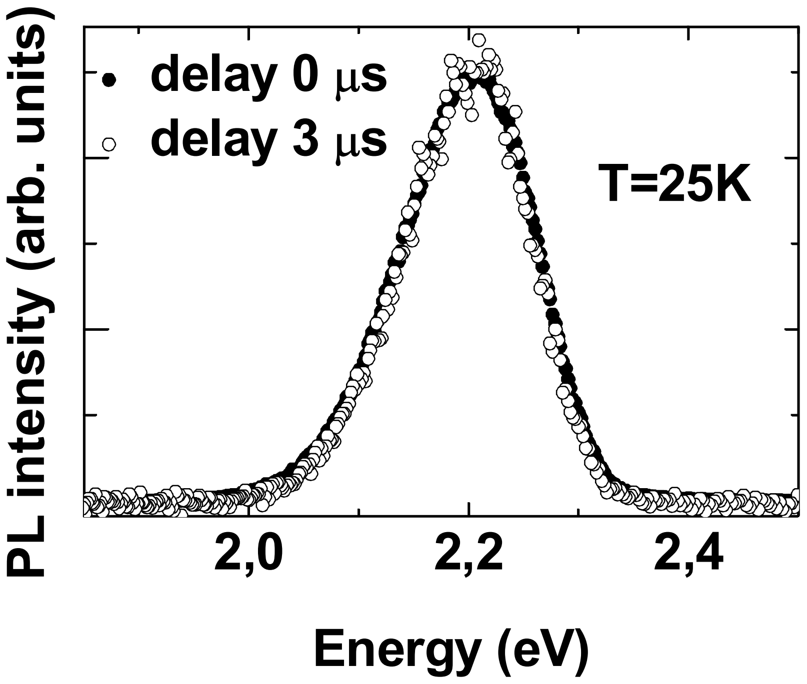

Figure 1: time resolved PL spectra recorded in the μs time domain

PL time decays recorded at different temperatures are shown in figure 2 in a semi-log plot. Experimental data show that at temperatures below 290 K, the fluorescence decay is characterized by a non-exponential tail whose contribution increases with decreasing temperature. PL life-time of 670±20 ns was measured at 290 K by assuming a single exponential decay. The analysis of the decay curves at lower temperatures performed in the 0-1μs delay range, where a single exponential decay is observed, indicates that the PL lifetime does not depend on the temperature in this range.

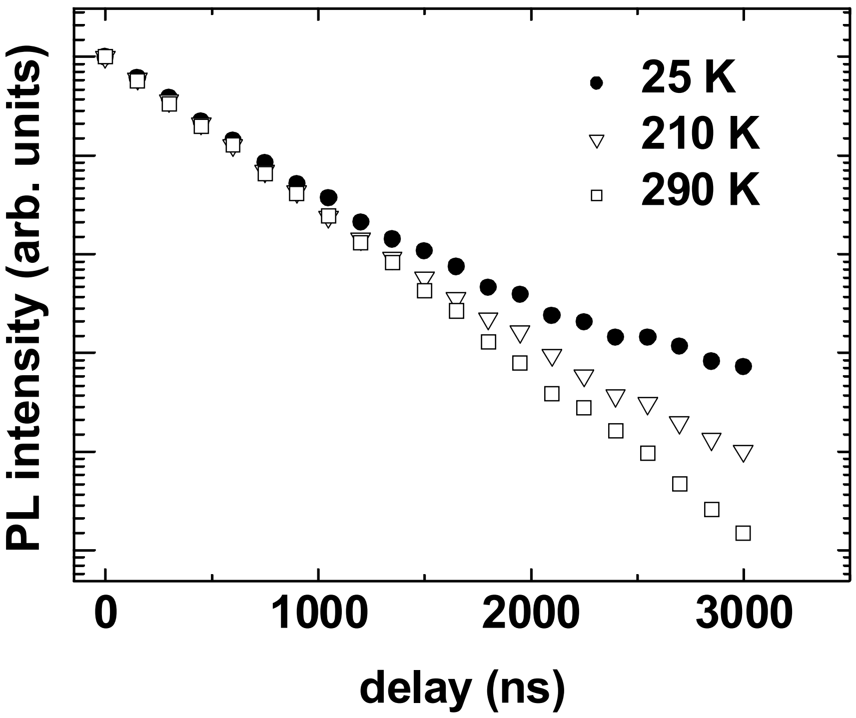

Figure 2: PL decay measurements as a function of increasing temperature

PP decay measured at 9 K in the 0-10^3 s time domain is shown in figure 3. Experimental data can be fitted with a first order exponential decay with an measured decay constant of 420 s. PP spectrum, recorded 1 minute after the excitation pulse reported in the inset of fig. 3, shows that spectral position and shape of the emission resembles the Eu^{2+} fluorescence recorded in the μs range (see fig. 1)

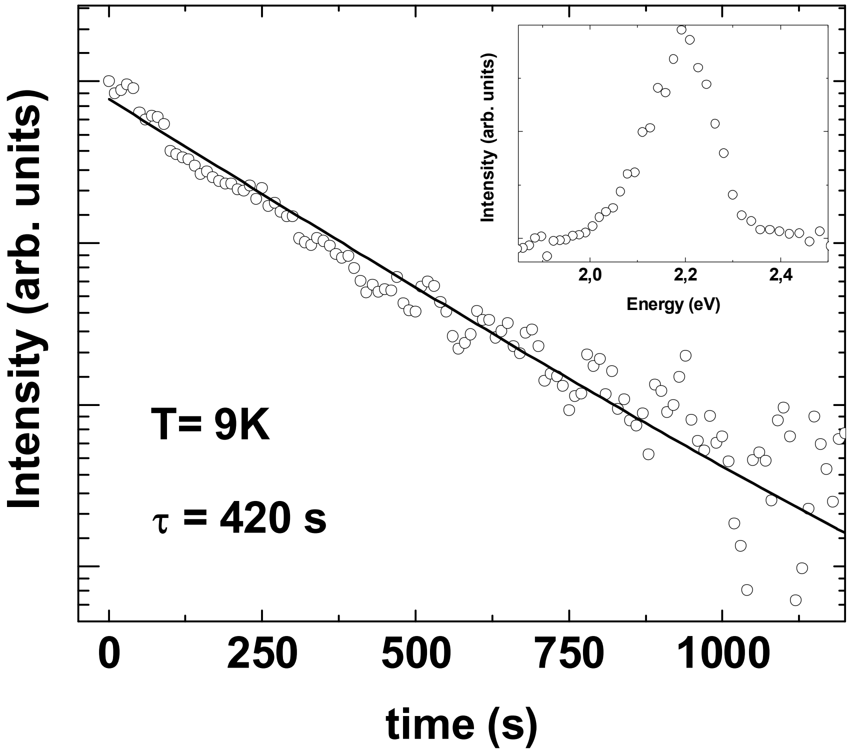

Figure 3: PP decay curve and emission spectrum (inset) recorded at 9 K

The TL glow-curve is shown in figure 4, where the TL intensity integrated in the 1.9-2.4 eV range is plotted as a function of increasing temperature. The glow curve is composed of two peaks at 69 and 98 K and by a large TL band at about 185 K (A, B and D respectively in fig. 4). Two other shoulders superimposed on the band at 185 K are observed at 145 and 244 K respectively (C and E respectively in fig. 4).

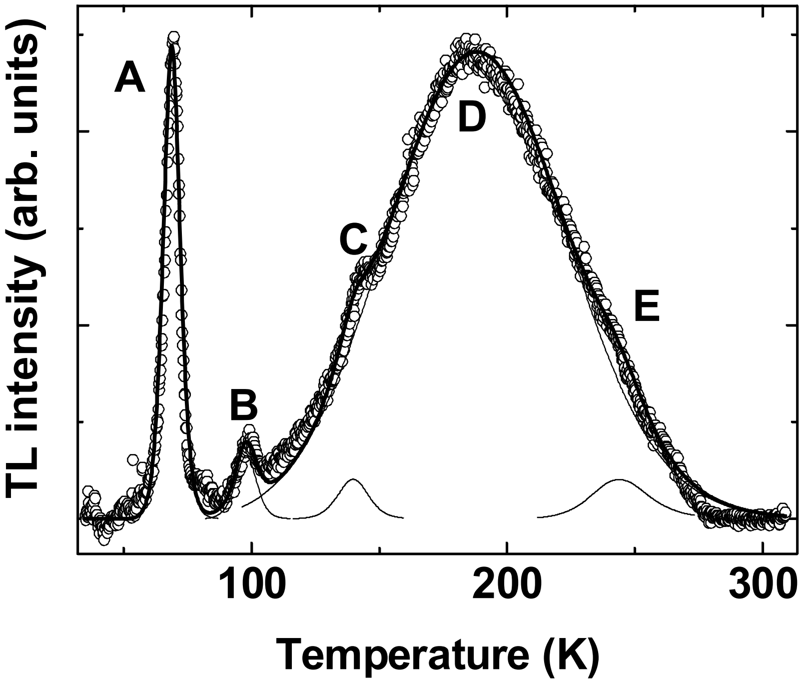

Figure 4: TL glow curve and curve fitting result (open circle: experimental data; thick solid line: curve fitting according to eq. (2); thin lines: curve-fitting components)

The spectral distribution of thermally stimulated emissions recorded at the glow-curve main maxima is shown in figure 5. As previously observed for the PP emission (see fig. 3) the glow-emission resembles the Eu^{2+} fluorescence recorded in the μs range (see fig. 1).

In order to better investigate the broad TL band peaked at 185 K, phosphorescence decays carried out at few selected temperatures (100, 185 and 288 K) are shown in figure 6. As indicated by the different slopes of experimental data reported in a log-log plot, the observed long lasting fluorescence decrease as $t^{-\alpha}$, with $\alpha = 1.0 \pm 0.1$, 0.8 ± 0.1, 1.8 ± 0.1, at 100, 185 and 288 K respectively.

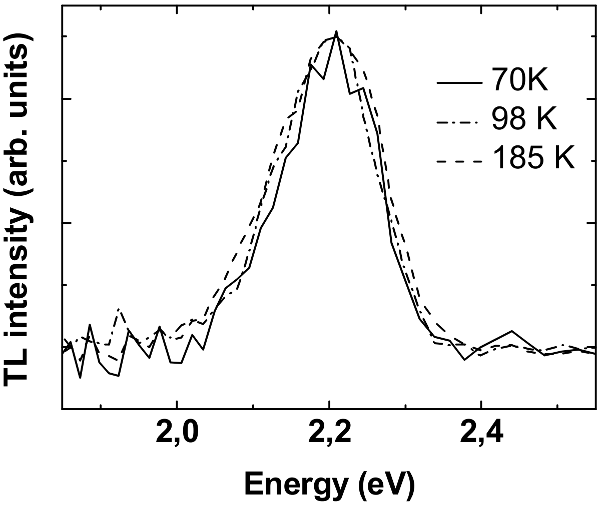

Figure 5: TL emission spectra recorded at different temperatures

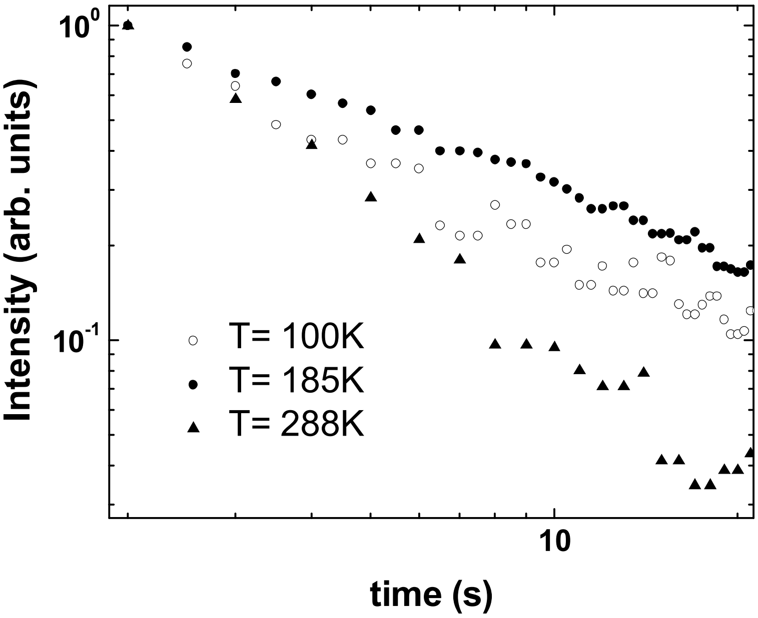

Figure 6: PP decay curve at different temperatures

6.2 Discussion

The reported data can be summarized as follows:

a) time resolved PL spectra of $CaGa_2S_4$:Eu^{2+} recorded in the μs range are characterized by the well known emission of Eu^{2+} at 564 nm and the Eu^{2+} PL decays as a single exponential law with a lifetime of 670 ns;

b) at low temperature, a non-exponential tail is observed in the PL decay, whose relative weight decreases with increasing temperature;

c) $CaGa_2S_4$:Eu^{2+} exhibits PP and TL emissions, whose spectral properties resemble that of PL emission;

d) PP decays as a single exponential at 9K and as a power law at higher temperatures;

Since the deviation from a single exponential decay is not accompanied by variations in the spectral distribution (see fig. 1), we can assume that the Eu^{2+} PL band-shape is characterized by homogeneous broadening. Therefore the observed non-exponential tail cannot be ascribed to a stretched distribution of active ions, but rather to the persistence of the emission which could be related to the presence of trapping defects. This hypothesis is confirmed by the spectral distribution of long lasting emissions (see figures 3 and 5) as compared to Eu^{2+} PL recorded in the μs range (see fig. 1). Moreover the increase of the full width at half maximum (FWHM) with increasing temperature calls for the vibronic nature of Eu^{2+} emission. This indicates that charge carriers thermally released by traps radiatively recombine at Eu^{2+} sites. In particular at 9 K (see fig. 3) the PP shows a single exponential decay which is indicative of monomolecular kinetic [8], in agreement with the hypothesis of trapping levels localized close to Eu^{2+} sites.

According to the generalized order of kinetic model of thermoluminescence (GOK), the glow curve intensity as a function of temperature can be described by the ensuing equation [8]:

$$I(T) = A \cdot S \exp\left(-\frac{E}{kT}\right)\left[1 + \frac{(b-1)S}{\beta}\int_{T_1}^{T_2} \exp\left(-\frac{E}{kT}\right) dT\right]^{-\frac{b}{b-1}} \qquad (1)$$

where A is a scale constant, which depends on the traps concentration, E is the trap depth (the energy needed to release the trapped charge carrier), k is the Boltzmann's constant, b and S are phenomenological parameters related to the trapping kinetics and frequency factor respectively, and β is the sample heating rate [8]. By applying the GOK model to the TL glow curve presented in figure 4, we assumed that the full glow curve is described by the superposition of five components, i.e.:

$$I(T) = \sum_{j=1}^{5} A_j \cdot S_j \exp\left(-\frac{E_j}{kT}\right)\left[1 + \frac{(b_j-1)S_j}{\beta}\int_{T_1}^{T_2} \exp\left(-\frac{E_j}{kT}\right) dT\right]^{-\frac{b_j}{b_j-1}} \qquad (2)\ .$$

A good fitting result (the solid line in figure 4) was achieved with the parameters summarized in table I (square correlation factor $R^2 = 0.97$).

According to the fit, the glow curve components at 69, 98, 145 and 244 K (A, B, C and E in fig. 4) are characterized by trap depths of 156, 260, 370 and 650 meV respectively, with frequency factor ranging from 10^{10} to 10^{12} s^{-1}. The TL band at 185 K (D in fig. 4), is characterized by a trap depth of 74 meV and S=0.5, which are comparable to previously reported values [9,10].

component	glow peak (K)	E (meV)	S (s^{-1})	b
A	69.0± 0.5	150±10	$\sim10^{10}$	~1.7
B	98.0± 0.5	260±10	$\sim10^{12}$	~1.7
C	145.0± 0.5	370±30	$\sim10^{12}$	~1.7
D	185.0± 0.5	74±1	$\sim10^{-2}$	~1.2
E	244.0±0.5	650±5	$\sim10^{12}$	~2

Table I: main thermoluminescence parameters derived from GOK analysis

The relatively small value of the FWHM of the A, B, C and E components indicates a small degree of disorder and suggests that these glow peaks are due to trap levels with sharp distribution. It is well know that Eu^{2+} ions substitutes Ca ions in three different crystallographic sites [10]. Alternatively it is possible that a fraction of the doping ions occupies interstitial positions in the neighbours of Ca ions. In both substitutional or interstitial cases, the presence of Eu^{2+} induces strain lattice or point defects in the local environment due to the differences between the lanthanide and alkaline-earth properties (ionic radius, mass, electro-negativity) and produces the trapping levels related to the glow components.

Regarding the D component, the obtained value of the frequency factor is significantly smaller than typical Debye frequencies. This abnormality usually calls for a reappraisal of the simple concept of thermal stimulation from a trap [8]. In the past the anomalous small value of the *S* parameter in co-doped samples was attributed to thermal quenching [9]. On the other hand a wide TL band in the 100-250 K range was observed in $CaGa_2S_4$:Eu^{2+} and attributed to a continuous distribution of traps with activation energies ranging from 100 to 300 meV [10]. It was also pointed out that for a given distribution of defects, PP intensity decays as $t^{-\alpha}$ with the α value depending on the actual distribution [8]. PP decays data (see fig. 5) displayed that in the 100-300 K temperature range the α value varies in a non-monotonic way between 0.8 and 1.8, thus indicating that the presence of defect distributions cannot be excluded. Therefore we conclude that the glow band at 185 K is not due to thermal release by a single trap, but rather to a continuous distribution of defects with maximum at about 74 meV from one of the band edges. This hypothesis is confirmed by the general properties of ternary compounds which are known to be characterized by distribution of defects which can act as electron trapping centres [11-12].

6.3 Review of the Main Results

The phosphorescence and thermoluminescence properties of $CaGa_2S_4$:Eu^{2+} in the 9-325 K temperature range were discussed. Samples exhibited long lasting emission at low temperature with a lifetime of 420 s measured at 9K. Thermoluminescence in the 35-325 K temperature range is characterized by five components at 69, 98, 145, 244 and 185 K and the corresponding trap depths were estimated according to the GOK model. Because of their sharp distribution, activation energies of 156, 260, 370 and 650 meV were attributed to defects induced by the inclusion of Eu^{2+} ions in the three different Ca sites and to interstitial defects. The glow band at 185 K was attributed to a continuous distribution of defects with maximum at 74 meV from one of the band edges.

The comparison between the spectral properties of photoluminescence, phosphorescence and thermoluminescence shows that long lasting emissions occur at Eu^{2+} sites, indicating that the energy stored in the trapping defects is thermally transferred to the lanthanide ions.

References

[1] C. Chartier, R. Jabbarov, M. Jouanne, J. Morhange, P. Bernalloul, C. Barthou, J. Frigerio, B. Tagiev, and E. Gambarov, J. Phys.: Condensed Matter 14, 13693 (2002).

[2] C. Chartier, P. Barnalloul, C. Barthou, J. Frigerio, G. O Muller, R. Mueller-March, and T. Trittier, J. Phys. D: Appl. Phys. 35, 363 (2002).

[3] K. Tanaka, Y. Inoue, S. Okamoto, K. Kobayashi, and K. Takizawa, Jpn. J. Appl. Phys., Part 1 n° 6A 36, 3517 (1997).

[4] A. N. Georgobiani, A. N. Gruzintsev, C. Barthou, P. Bernalloul, J. Benoit, B. G. Tagiev, O. B. Tagiev, and R. B. Dzhabbarov, J. Electrochem. Soc. 148, H167 (2001).

[5] M. C. Nostrand, et al., Opt. Lett. 24, 1215 (1999).

[6] Yurii V. Orlovskii, Tasoltan T. Basiev, Konstantin K. Pukhov, Maxim E. Doroshenko, Valery V. Badikov, Dmitry V. Badikov, Olimkhon K. Alimov, Marina V. Polyachenkova, Leonid N. Dmitruk, Vyacheslav V. Osiko, Sergey B. Mirov - Optical Materials 29 (2007) 1115–1128

[7] T. E. Peters and J. A. Baglio, J. Electrochem. Soc.: Solid-State Science and Technology 119, 230 (1972).

[8] S.W.S. McKeever "Thermoluminescence of Solids" - Cambridge University Press 1985 – chapter 3 pp 20-64

[9] H. Najafov, A. Kato, H. Toyota, K. Iwai, A. Bayramov, S. Ida, Jpn. J. Appl. Phys. Vol 41 (2002) pp 2058-2065

[10] P. Benalloul, C. Barthou, C. Fouassier, A. N. Georgobiani, L. S. Lepnev, Y. N. Emirov, A. N. Gruzintev, B. G. Tagiev, O. B. Tagiev, R. B. Jabbarov, Journal of Elettrochem. Soc. 150 (1) G62-G65 (2003)

[11] P.C. Ricci, A. Anedda, R. Corpino, I. M. Tigynianu, V. V. Ursaki J. Phys. Chem. Sol. 64 (2003), pp. 1941-1947

[12] A. Serpi, J. Phys. D: Appl. Phys., Vol. 9, 1976 pp. 1881-1892

Chapter 7:

Energy Transfer in Ce and Eu Codoped Barium Thiogallate

In this chapter the fluorescence properties of Ce^{3+} *single-doped and* Ce^{3+}/Eu^{2+} *co-doped* $BaGa_2S_4$ *crystals are reported. The comparison between the emissions observed in single and co-doped samples shows that* Ce^{3+} *PL is strongly influenced by* Eu^{2+} *co-doping The reported data are discussed in the framework of energy transfer process between Ce and Eu. The rate of the energy transfer was estimated in* $7.5 \cdot 10^7$ s^{-1} *with efficiency of 66%.*

7.1 Experimental details

Room temperature photoluminescence measurements were performed with excitation provided by the MOPO emission at 310 nm (3.99 eV). Spectra were collected with a spectral bandwidth of 2 nm. Depending on PL bands under examination, different delays from excitation pulse and time gates were used. The temporal response function of the detection system was determined.

7.2 Results and Discussion

The photoluminescence spectrum of $BaGa_2S_4$:Ce is shown in figure 1. The PL band is peaked at 448 nm and two shoulders are observed in the 380-420 and 470-490 nm spectral ranges. The components at 448 nm and 470-490 nm arise from Ce^{3+} radiative transitions from the ^2D level to the $^2F_{5/2}$ and $^2F_{7/2}$ levels respectively [1,2]. The third component at 380-420 nm could be explained as a radiative transition from the E_g level to the ground state of Ce^{3+} ions [3].

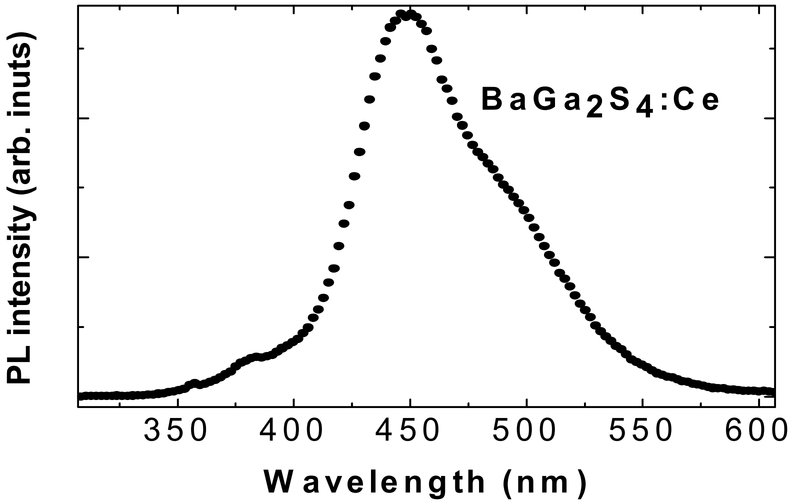

Figure 1 : Room temperature time resolved PL spectrum of $BaGa_2S_4$:Ce. Gate width 10 ns, delay 15 ns.

The PL spectrum of $BaGa_2S_4$:Ce,Eu is shown in figure 2. The observed spectrum is composed by a band peaked at 500 nm and attributed to Eu^{2+} radiative transition from the $4f^6d$ state to the ground state [1,4], and a weaker band at about 410 nm. The Ce^{3+} main emission at 448 nm is strongly quenched, while the only contribution that can be ascribed to cerium ions is the emission in the 380-420 nm range [3]. Indeed no emissions in the 400-440 nm range have been previously reported in Eu^{2+} single doped samples [1, 4]

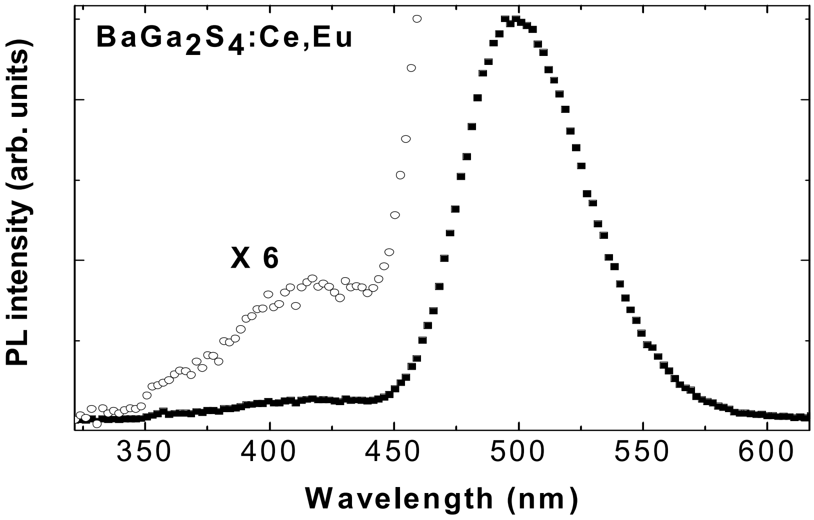

Figure 2 : Room temperature time resolved PL spectrum of $BaGa_2S_4$:Ce,Eu (full squares) and magnified intensity for the spectral components around 410 nm (open circles). Gate width 10 ns, delay 5 ns.

The time decay of the Ce^{3+} fluorescence in the single doped samples are shown in figure 3. All PL decay measurements were performed in a time domain comparable to the excitation pulse width and therefore convolution effects cannot be neglected. By assuming a single exponential decay, the fluorescence signal is described by the ensuing equation [5] :

$$I(t) = \int_0^t A\, L(x) \exp(-\frac{t-x}{\tau}) dx \qquad (1)$$

were A is a scale constant, *L(x)* is the excitation time profile and τ is the fluorescence lifetime. The convolution technique allows the measurement of fluorescence lifetime with good accuracy, provided that the time response of the detection system is known and that a realistic hypothesis on the fluorescence decay law could be advanced [6]. In the following all fitting results are reported with errors estimated at a confidence level of 99%.

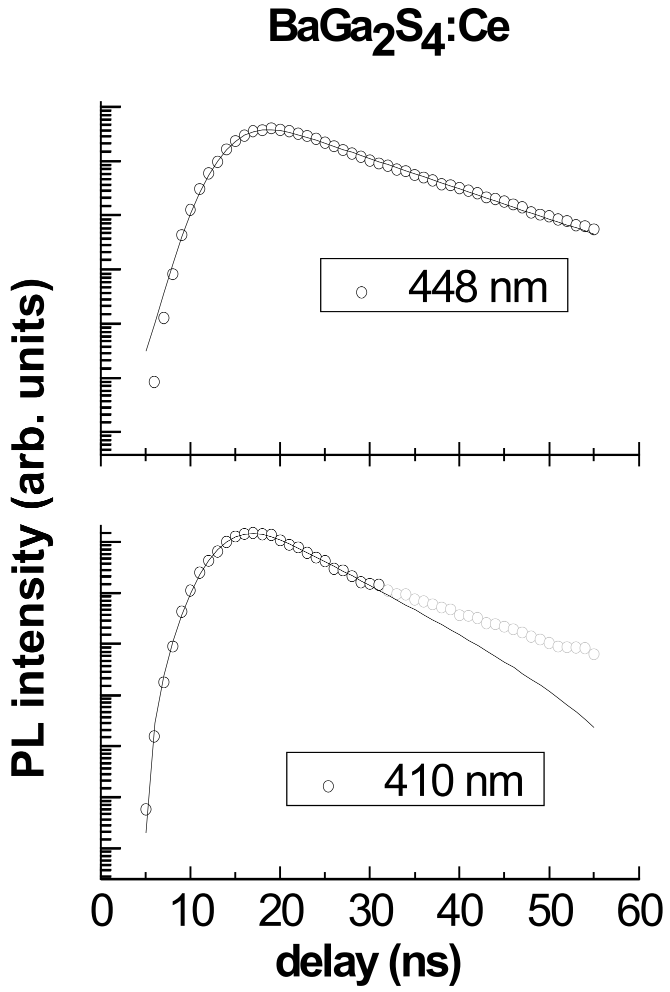

Figure 3: PL time decays of $BaGa_2S_4$:Ce (open circles). The continuous line is the curve-fitting result

We performed a curve-fitting analysis on experimental data using eq. (1) for Ce^{3+} emissions in the single doped sample. Fluorescence lifetime of (11 ± 2) ns and (18± 2) ns were obtained monitoring at 410 and 448 nm respectively. These values are comparable with previously reported Ce^{3+} fluorescence lifetime in similar compounds [7,3] . The different decay time constants of the 410 and 448 nm emissions confirm that these two emissions originate from excited states of Ce^{3+} with different symmetries.

Time decays of Ce^{3+} fluorescence recorded at 410 nm for the single and co-doped samples are compared in figure 4 in a semi-log plot. As shown by the different slopes of the two curves in the 20-30 ns range, the Ce^{3+} fluorescence in the presence of Eu^{2+} co-doping is faster than in the case of single doping. It is possible to estimate the lifetime of the emission in co-doped samples with a single exponential curve fitting in the 22-35 ns range, where the excitation pulse intensity is negligible: the estimated lifetime was (6 ± 3) ns (square correlation factor R^2>0.66).

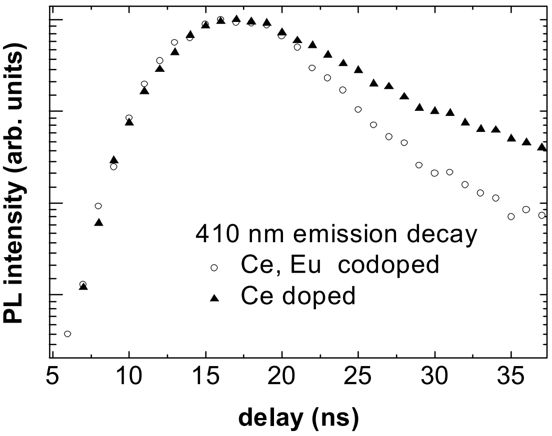

Figure 4: Time decays of Ce emissions at 410 nm in single and co-doped sample

In order to check and improve this result we have also performed the analysis by means of convolution curve-fitting technique [5]. Fluorescence time decay analysis for the co-doped samples is shown in figure 5. According to eq. (1) we estimated a lifetime for Ce^{3+} emission monitored at 410 nm of (6 ± 2) ns. This result indicates that a de-convolution can be performed with good accuracy also when the measured lifetime is comparable with the pulse excitation width, as already reported [7, 5].

Time decays of the Eu^{2+} fluorescence at 500 nm for the codoped samples are shown in figure 5. From experimental data analysis with equation (1) we estimated a lifetime of (290 ± 5) ns which is in agreement with previous determinations [4].

In order to verify the quenching of the Ce^{3+} emission at 448 nm in the co-doped samples, we measured the fluorescence decay gathered at 448 nm (fig. 5). In the 25-60 ns range, data resemble the Eu^{2+} decay while a different rate is observed from 20 to 25 ns, thus indicating a composite nature of the monitored emission. Therefore we assumed a second order exponential decay for the convolution integral :

$$I(t) = \int_0^t L(x) \cdot \left[A\exp(-\frac{t-x}{\tau_1}) + B\exp(-\frac{t-x}{\tau_2}) \right] dx \qquad (2)$$

were *L(x)* is the excitation time profile, *A* and *B* are the amplitudes of the two emissions decay, τ_1 and τ_2 are the fluorescence lifetimes. We found τ_2 = (290 ± 20) ns which is the europium fluorescence lifetime, and τ_1 = (6 ±

2) ns . Regarding the value of τ_1 it can be explained as the lifetime of Ce^{3+} emission at 448 nm strongly affected by Eu^{2+} co-doping.

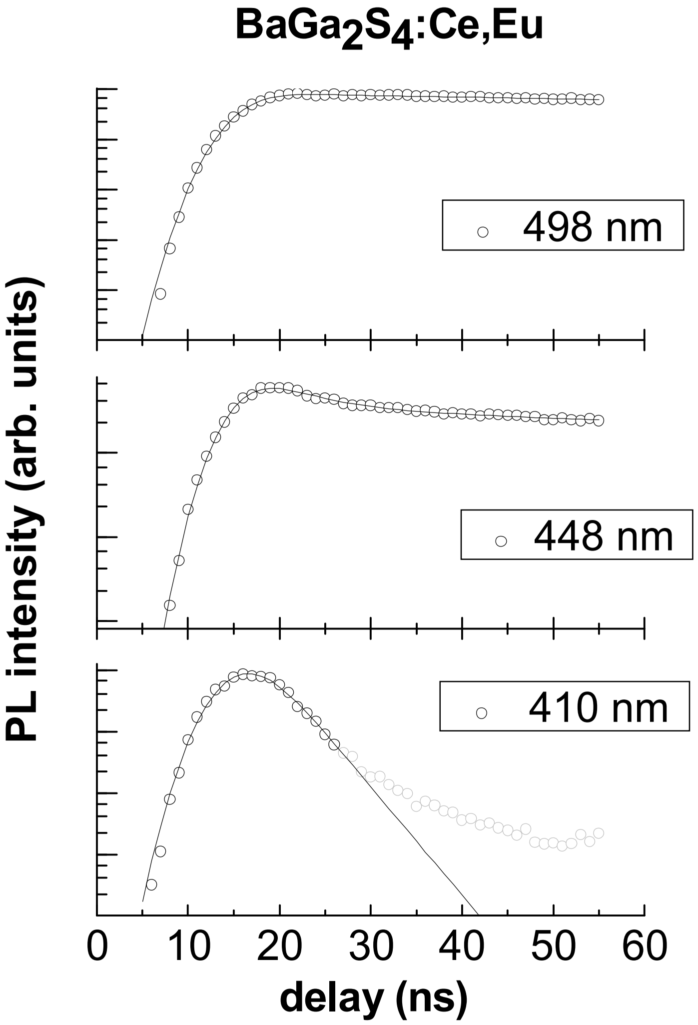

Figure 5: PL time decays of $BaGa_2S_4$:Ce,Eu (open circles). Continuous lines are the curve-fitting results

Our analysis shows that the Ce^{3+} fluorescence is faster in the co-doped samples than in single-doped ones. It should be pointed out that the decrease in fluorescence lifetime can be ascribed to the presence of defect induced by the large value of dopant concentration (3%). In this case, however, not only the Ce^{3+} fluorescence lifetime should be shortened but also the Eu^{2+} PL lifetime should decrease. Therefore we conclude that the observed decrease in Ce^{3+} lifetime cannot be ascribed to the presence of induced defects. On the other hand, the decrease of the fluorescence lifetime could be ascribed also to an increase of the non radiative transition rate because of co-doping. It was recently established that Raman spectra of thiogallate compounds are almost independent on the cation nature [8]: differences in the order of a fraction of cm^{-1} were observed in Raman spectra, also when the rare earth totally substitutes the cation. This indicates that the energy of the mean phonon coupled with the emitting centre does not vary meaningfully with co-doping. Therefore the observed decreasing in Ce^{3+} lifetime should be ascribed to interactions taking place between Ce^{3+} and Eu^{2+}.

In the past the decrease of the cerium lifetime was observed in calcium thiogallate codoped with europium and explained with a resonant energy transfer, with Ce^{3+} ions acting as sensitizers for Eu^{2+} [7]. According to this model the energy transfer rate is given by [7]:

$$W = \frac{1}{\tau} - \frac{1}{\tau_0} \quad (3)$$

with efficiency of the energy transfer equal to $W\tau$ [9], where τ is the Ce^{3+} lifetime in co-doped samples and τ_0 the lifetime in single doped sample. According to eq. (3) we estimated an energy transfer rate of $7.5 \cdot 10^7$ s^{-1} with efficiency of 66%, that is comparable with the rate observed in calcium thiogallate [7]. Assuming an energy transfer efficiency of 66 % at 410 nm and taking into account that the europium absorption maximum is at 453 nm [10], the decreased lifetime at 448 nm in co-doped sample could be explained with a more efficient energy transfer from Ce^{3+} to Eu^{2+}. In order to verify this hypothesis measurements as a function of dopant's concentration are mandatory. Further measurements are in progress in order to verify whether the observed energy transfer enhances the quantum yield of Eu fluorescence or not.

7.2 Review of the Main Results

The fluorescence properties of $BaGa_2S_4$:Ce and $BaGa_2S_4$:Ce,Eu were discussed. To the best of our knowledge this is the first report concerning the PL properties of $BaGa_2S_4$:Ce,Eu. Ce^{3+} fluorescence lifetime measured at 410 nm decreased from 11 ns in single-doped sample to 6 ns in the presence of Eu^{2+} co-doping. This trend was explained with an energy transfer process between Ce and Eu. The rate of the energy transfer at 410 nm was estimated in $7.5 \cdot 10^7$ s^{-1} with an efficiency of 66%. In order to better investigate the observed energy transfer between Ce^{3+} and Eu^{2+}, a detailed study as a function of dopant's concentration is necessary.

References

[1] T.E. Peters and J.A. Baglio, J. Electrochem. Soc.: SOLID STATE SCIENCE AND TECHNOLOGY, VOL 119, n° 2 (1972), pp 230-235

[2] P. Dorenbons, Journal of Luminescence vol 91 (2000), pp. 155-176

[3] A. Kato, M. Yamazaki, H. Najafov, K. Iwai, A. Bayramov, C. Hidaka, T. Takizawa, S. Ida, J. Phys. Chem. Solids 64 (2003), pp. 1511-1517

[4] R.B. Jabbarov, C. Chartier, B.G. Tagiev, O.B. Tagiev, N.N. Musayeva, C. Barthou, P. Benalloul J. Phys. Chem. Solids 66 (2005), pp. 1049-1056

[5] J.R. Lakowicz, Principles of Fluorescence Spectroscopy, 2nd edition, chap. 4 pp 103- Kluwer 1999

[6] Topics in Fluorescence Spectroscopy vol 1: Techniques – chap. 1, pp 14-22 Edited by Joseph R. Lakowicz – Kluwer 2002

[7] H. Najafov, A. Kato, H. Toyota, K. Iwai, A. Bayramov, S. Ida, Jpn. J. Appl. Phys. Vol 41 (2002) pp. 1424-1430-Part 1 n° 3A

[8] C. Charter, R. Jabbarov, M. Jouanne, JF. Morhange, P. Beballoul, C. Barthou, JM Frigerio, B. Tagiev, E. Gambarov, J. Phys.: Condensed Matter, 14 (2002), pp. 13693-13703

[9] H. Lin, X. R. Liu, E. Y. B. Pun, Opticals Materials 18 (2002), pp. 397-401

[10] P. Dorenbons, Journal of Luminescence 104 (2003) pp. 239-260

Conclusions

The subject of this Ph. D. thesis was the characterization of the fluorescence properties of wide band gap compounds doped with lanthanide ions. Due to their attractive properties for photonics and optoelectronics applications alkaline earth thiogallates were chosen as the host matrix. Indeed the good transmission properties in the visible part of the electromagnetic spectrum and the relatively low phonon energy of these materials allow high efficiency photoluminescence, while the electrical conduction properties are useful for electro-luminescence applications. The alkaline earth thiogallates can be doped with lanthanide ions, also in large concentrations, because of the close similarity of the ionic radius of alkaline earth and lanthanide ions. Moreover these materials are chemically and environmentally stable and can be grown also with low cost techniques, thus appearing as promising materials for technological applications.

The samples studied in this work were grown with a solid state reaction technique at the Institute of Physics of Azerbaijan Academy of Sciences. Several set of polycrystalline samples were grown with nominal dopant concentration as follows: $CaGa_2S_4$:Ce^{3+}, Pr^{3+} (both Ce^{3+} and Pr^{3+} at 2% atm) ; $CaGa_2S_4$:Eu^{2+} (Eu^{2+} at 2% atm) ; $BaGa_2S_4$:Ce^{3+}(Ce^{3+} at 3% atm) ; $BaGa_2S_4$:Ce^{3+}, Eu^{2+} (both Ce^{3+} and Eu^{2+} at 3% atm).

In order to improve the technological applications of REE doped thiogallate compounds the investigation of the interaction of the REE ions and the host matrix is a fundamental task. The experimental study was focused on three main issues: the interactions between the rare earth elements (REE) and the thiogallate matrix; the interactions between the REE and the defects of the host; the interactions between REE in codoped samples. The study was performed by means of time resolved photoluminescence measurements as a function of temperature in the 10-335 K range and at different excitation wavelengths. Time resolved PL measurements as a function of temperature allowed to characterize the PL kinetics and the PL band shape, thus providing informations about the interactions between the REE and the host matrix, and to characterize the environment of the optically active centres and the nature of the electron phonon coupling. Moreover the analysis of PL decays allows to investigate the interactions between REE ions or between the optically active centres and the defects of the host matrix. In particular, the interactions with host defects were investigated by means of phosphorescence (PP) and thermoluminescence (TL) measurements.

The main experimental results are listed in the following:

- **$CaGa_2S_4$:Eu^{2+}**: Eu^{2+} PL band is peaked at 2.21 eV at 9K with a FWHM of 140 meV and a lifetime of 453 ns. The PL band is characterized by a medium strength electron-phonon coupling (Huang-Rhys parameter value of 5) with effective phonon energy of 25-27 meV; the Stokes shift was evaluated in 225 meV. As the temperature increases the PL intensity decreases and the fluorescence lifetime increases, due to the thermal population of a metastable level of the 4f5d Eu^{2+} manifold, which lies at about 60 meV from the lowest 4f5d state.

- **$CaGa_2S_4$:Ce^{3+}, Pr^{3+}** : the photoluminescence properties of this type of co-doping in calcium thiogallate at room temperature were investigated for the first time. PL components arising from Ce and Pr centres were spectrally resolved by means of time resolved spectroscopy. Ce and Pr emissions were found to be in agreement with previous studies performed on samples doped with a species alone, suggesting that the general spectroscopic features are not effected by the coexistence of the two dopants, as also confirmed by the measured lifetime of Ce and Pr fluorescence. These results suggest a possible application in tuning the colour emission of the phosphor. A band at 2.2 eV was observed for the first time, which affects the time decay behaviour of Ce PL.
- **$CaGa_2S_4$:Eu^{2+}**: the samples exhibited long lasting emission at low temperature with a lifetime of 420 s measured at 9K. Thermoluminescence in the 35-325 K temperature range is characterized by five components at 69, 98, 145, 185 and 244 K and the corresponding trap depths were estimated according to the GOK model. The glow components at 69, 98, 145 and 244 K with activation energies of 156, 260, 370 and 650 meV were attributed to defects induced by the substitutional inclusion of Eu^{2+} ions in the

three different Ca sites and to interstitial defects. The glow band at 185 K was attributed to a continuous distribution of defects with maximum at 74 meV from one of the band edges. The comparison between spectral properties of photoluminescence, phosphorescence and thermoluminescence shows that long lasting emissions occur at Eu^{2+} sites, indicating that the energy stored in the trapping defects is thermally transferred to the lanthanide ions.

- **$BaGa_2S_4:Ce^{3+}$** and **$BaGa_2S_4:Ce^{3+},Eu^{2+}$**: to the best of our knowledge this is the first report on the energy transfer in Ce and Eu co-doped barium thiogallate. Ce^{3+} fluorescence lifetimes measured at 410 nm decreased from 11 ns in single-doped sample to 6 ns in presence of Eu^{2+} co-doping. This trend was explained with an energy transfer process between Ce and Eu. The rate of the energy transfer at 410 nm was estimated in $7.5 \cdot 10^7$ s^{-1} with an efficiency of 66%.

As a natural continuation of this work the following issues should be investigated: i) regarding calcium thiogallate co-doped with cerium and praseodimium, no interactions between the ions was observed at room temperature. In order to verify if interaction effects are masked by temperature effects, low temperature measurement are necessary and would also allow to investigate the hyperfine structure of Pr^{3+} fluorescence; ii) concerning the thermoluminescence properties observed in $CaGa_2S_4:Eu^{2+}$ it would be interesting to investigate the effect of co-doping on the brightness and persistence of the long lasting emissions; iii) as regards the observed energy transfer in the co-doped sample of barium thiogallate, the sample characterization as a function of dopant concentration and quantum efficiency measurements are mandatory in order to better investigate the kinetics of the energy transfer and to verify if the Eu fluorescence is effectively sensitised by Ce co-doping.

Appendix: Complementary Activities

Beside the research about rare earth doped thiogallates, further works were carried out within the Group of Optical Spectroscopy and the Cryogenics Laboratory of the Department of Physics of the University of Cagliari.

Regarding the research projects of the Group of Optical Spectroscopy, the structural and photoluminescence properties of rare earth doped YAG and LYSO crystals were investigated. In the first case iron inclusions in the YAG matrix were studied by means of time resolved photoluminescence measurements as a function of temperature. This study led to the characterization of iron electron-phonon coupling, which was investigated both in linear and quadratic approximation. Regarding LYSO crystals, the structural properties of Ce-doped samples were investigated by means of Raman scattering measurements as a function of temperature and allowed to characterize the effect of Ce inclusion on the unit cell properties. Moreover the photoluminescence properties of LYSO:Ce were investigated with particular interest for the Ce excitation channels. The experimental study on YAG and LYSO crystals also involved two beam time sessions at Superlumi station at the HasyLab laboratory of the Deutsches Elektronen-Synchrotron (DESY) in Hamburg, where synchrotron radiation excited photoluminescence measurements were performed. These works were supported by the European Community - Research Infrastructure Action under the FP6 "Structuring the European Research Area" Programme (through the Integrated Infrastructure Initiative "Integrating Activity on Synchrotron and Free Electron Laser Science".) Contract RII3-CT-2004-506008.

An other project concerned the characterization of the photo-stability properties of organic-inorganic hybrids of interest as solid state active media for laser applications. In particular porous SiO_2 activated with Rhodamine 6G samples, obtained by sol-gel technique, were investigated by means of photoluminescence measurements as a function of the excitation power density on the samples and as a function of the irradiation time. In this study it was established that samples obtained by Rhodamine perchlorate exhibit the better long-term stability properties.

Moreover, in collaboration with the colleagues of the Photonics and Optoelectronics Group of The Department of Physics of University of Cagliari, the lasing properties and non-linear losses of nano-fibers were investigated by means of time resolved photoluminescence measurements on the ns scale.

Regarding the activities within the Cryogenics Laboratory, a contribution was given to the production and supply of liquid helium for research purposes.

List of Publications

Temperature tuning of lasing threshold in self-assembled oligophenyl nanofibers under nanosecond optical excitation
F. Quochi, M. Saba, F. Cordella, A. Gocalinska, R. Corpino, M. Marceddu, A. Anedda, A. Andreev, H. Sitter, N.S. Sariciftci, A. Mura, e G. Bongiovanni
Submitted to *Advanced Functional Materials*

Low Temperature Thermoluminescence in $CaGa_2S_4$:Eu^{2+}
A. Anedda, C.M. Carbonaro, R. Corpino, M. Marceddu, A.N. Georgobiani, O. B. Tagiev
Submitted to *Journal of Luminescence*

Energy Transfer in Ce and Eu co-doped Barium Thiogallate
M. Marceddu, A. Anedda, R. Corpino, A.N. Georgobiani, P.C. Ricci
Material Science and Engineering B Vol 146/1-3 (2008) pp 216-219

Ce^{3+}-doped lutetium yttrium orthosilicate crystals: Structural Characterization
Pier Carlo Ricci, Carlo Maria Carbonaro, Daniele Chiriu, Riccardo Corpino, Nicola Faedda, Marco Marceddu and Alberto Anedda
Material Science and Engineering B vol 146 (2008) 2–6

Time Resolved Photoluminescence of Eu 4f5d manifold in calcium thiogallate
A. Anedda, R. Corpino, M. Marceddu, A. N. Georgobiani, B.G. Tagiev and O.B. Tagiev
Conference Proceedings Vol. 94 "*Highlights on Spectroscopies of Semiconductors and Nanostructures*" Edited by G. Guizzetti, L.C. Andreani, F. Marabelli and M. Patrini- pp. 9-18 published b y Società Italiana di Fisica, Bologna Italy, June 2007

Electron-phonon coupling in iron-doped yttrium aluminum garnet
A. Anedda, C. M. Carbonaro, D. Chiriu, R. Corpino, M. Marceddu, and P. C. Ricci
PHYSICAL REVIEW B 74, 245108 (2006)

On the interaction between iron ions and crystalline field in Iron doped Yttrium Aluminum Garnet.
P.C. Ricci, D. Chiriu, C.M. Carbonaro, R. Corpino, M. Marceddu, and A. Anedda
HasyLab Annual Reports 2006, pp. 641-643

Photoluminescence of Ce and Pr codoped calcium thiogallate
Anedda A., Carbonaro C.M., Chiriu D., Corpino R., Marceddu M., Ricci P.C., Georgobiani A.N., Tagiev B.G., Tagiev, O.B., Abushev, S.A., Tiginyanu, I.M.
Physica Status Solidi C: Current Topics in Solid State Physics, 3 (8), pp. 2717-2721. (2006)

Donor-acceptor pairs and excitons recombinations in AgGaS2
Marceddu, M., Anedda, A., Carbonaro, C.M., Chiriu, D., Corpino, R., Ricci, P.C.
Applied Surface Science 253, pp. 300-305. (2006)

Photostability of porous silica - rhodamine 6G hybrid samples
Carbonaro C.M., Marceddu M., Ricci P.C., Corpino R., Anedda A., Grandi S., Magistris A
Materials Science and Engineering C, 26 (5-7), pp. 1038-1043. (2006)

Large Stoke-shifted photoluminescence in Rare Earth Doped Thiogallate crystals
M. Marceddu, C.M. Carbonaro, D. Chiriu, R. Corpino, P.C. Ricci, and A. Anedda
HasyLab Annual Reports 2005, pp. 417-418

Congress Participations:

Energy Transfer in Ce and Eu codoped Barium Thiogallate
Oral communication at E-MRS Spring Meeting, May 2007 Strasbourg France

Photoluminescence of Ce and Pr codoped calcium thiogallate
Poster session at International Conference on Ternary and Multinary Compounds ICTM 15, March 2006 Kyoto, Japan

Donor–acceptor pairs and excitons recombinations in AgGaS2
Poster session at E-MRS Spring Meeting, May 2005 Strasbourg, France

Photostability of porous silica–rhodamine 6G hybrid samples
Poster session at E-MRS Spring Meeting, May 2005 Strasbourg, France